

1 **Nucleation and growth of sub-3 nm particles in the polluted urban atmosphere of a megacity in**
2 **China**

3 Huan Yu^{1,2,*}, Luyu Zhou¹, Liang Dai¹, Wenchao Shen¹, Jun Zheng^{1,2}, Yan Ma^{1,2}, Mindong Chen^{1,2}

4 1. School of Environmental Science and Engineering, Nanjing University of Information Science and
5 Technology, Nanjing, China

6 2. Collaborative Innovation Center of Atmospheric Environment and Equipment Technology,
7 Nanjing University of Information Science and Technology, Nanjing, China

8

9 Corresponding authors: hyu@nuist.edu.cn

10

11 **Abstract**

12 Particle size distribution down to 1.4 nm was measured in the urban atmosphere of Nanjing, China in
13 spring, summer and winter during 2014-2015. Sub-3 nm particle event, which is equivalent to
14 nucleation event, occurred on 42 out of total 90 observation days, but new particles could grow to
15 cloud condensation nuclei (CCN)-active sizes on only 9 days. In summer, infrequent nucleation was
16 limited by both unfavorable meteorological conditions (high temperature and RH) and reduced
17 anthropogenic precursor availability due to strict emission control measures during the 2014 Youth
18 Olympic Games in Nanjing. The limiting factors for nucleation in winter and spring were
19 meteorological conditions (radiation, temperature, and RH) and condensation sink, but for the further
20 growth of sub-3 nm particles to CCN-active sizes, anthropogenic precursors again became limiting
21 factors. Nucleation events were strong in the polluted urban atmosphere. Initial $J_{1.4}$ at the onset and
22 peak $J_{1.4}$ at the noontime could be up to $2.1 \times 10^2 \text{ cm}^{-3} \text{ s}^{-1}$ and $2.5 \times 10^3 \text{ cm}^{-3} \text{ s}^{-1}$, respectively, during the

23 8 nucleation events selected from different seasons. Time-dependent $J_{1,4}$ usually showed good linear
24 correlations with a sulfuric acid proxy for every single event ($R^2 = 0.56 - 0.86$, excluding a day with
25 significant nocturnal nucleation), but the correlation among all the 8 events deteriorated ($R^2 = 0.17$)
26 due to temperature or season change. We observed that new particle growth rate did not increase
27 monotonically with particle size, but had a local maximum up to 25 nm h^{-1} between 1-3 nm. The
28 growth rate behavior was interpreted in this study as the solvation effect of organic activating vapor
29 in newly formed inorganic nuclei using nano-Köhler theory.

30

31 **1. Introduction**

32 New particle formation (NPF) is an important source of secondary aerosols in the atmosphere
33 (Seinfeld and Pandis, 2006). Field studies and model simulations have consistently shown that NPF
34 can enhance cloud condensation nuclei (CCN) concentrations and contribute significantly to the
35 global CCN production (Wiedensohler et al., 2009; Yue et al., 2011; Spracklen et al., 2008; Pierce
36 and Adams, 2009; Merikanto, 2009; Yu and Luo, 2009; Matsui et al. 2013). NPF is a two-stage
37 process consisting of formation of clusters and subsequent growth to detectable sizes (McMurry et
38 al., 2005; Zhang et al., 2012). Recently, chamber experiments have made substantial progress in
39 revealing the fundamental processes involved in particle nucleation and growth (Kirkby et al., 2011;
40 Almeida et al., 2013; Schobesberger et al., 2013; Riccobono et al., 2014; Ehn et al., 2014; Kürten et
41 al., 2014). However, consistent theories are still under investigation to quantify the processes
42 physically, chemically, and dynamically (Kulmala et al., 2013, 2014). For example, the identity and
43 physico-chemical properties of assisting vapors other than sulfuric acid (H_2SO_4) are uncertain so far.
44 It is also uncertain what mechanisms allow the assisting vapors to overcome strong Kelvin effect

45 over sub-3 nm particles. Existing mechanisms include condensation of extremely low volatility
46 organic compounds (Ehn et al., 2014), nano-Köhler activation (Kulmala et al., 2004a), heterogeneous
47 chemical reactions (Zhang and Wexler, 2002), heterogeneous nucleation (Wang et al., 2013), and
48 adsorption of organics on cluster surface (Wang and Wexler, 2013). However, the relative
49 importance of various mechanisms is unknown.

50 Direct measurements of size- and time dependent nucleation rate and growth rate in sub-3 nm
51 size range are important to constrain the relative contributions from different mechanisms and
52 precursors. Such measurements are also important to evaluate the survival probability of new particle
53 to CCN-active sizes (~100 nm for soluble particles at 0.2% super saturation, Pierce and Adams, 2009)
54 and to reveal the limiting factors in the process. Recently, a series of new instruments have been
55 developed to measure sub-3 nm aerosol number concentration and chemical composition, such as
56 condensation particle counters (e.g., PSM, DEG-SMPS, Jiang et al., 2011a; Sipila et al., 2009;
57 Vanhanen et al., 2011), ion spectrometers (e.g., NAIS, Asmi et al., 2009), and mass spectrometers
58 (e.g., Cluster-CIMS, APi-TOF, CI-APi-TOF, Jokinen et al., 2012; Junninen et al., 2010; Zhao et al.,
59 2010). Kuang et al. (2012) developed a de-coupling method to measure size- and time dependent
60 growth rates of sub-5 nm particles. Their results at two urban sites in U.S.A showed that
61 size-resolved growth rates increased approximately linearly with particle size from 1 to 5 nm.
62 Similar results were also observed in the Boreal forest (Kulmala et al., 2013; Lehtipalo et al., 2014).
63 Based on growth rates measured below 2 nm, Kulmala et al. (2013) identified three separate size
64 regimes, which were dominated by different key gas to particle conversion processes.

65 The relative contribution of different precursors and mechanisms to the nucleation and growth of
66 1-3 nm particles may vary greatly with atmospheric conditions (Riipinen et al., 2012). Therefore,

67 sub-3 nm particle measurements in a variety of atmospheric conditions, e.g., remote or urban
68 atmosphere, biogenic- or anthropogenic emission dominated areas, are immensely valuable.
69 Unfortunately, such data are very sparse until now (Jiang et al., 2011b; Kuang et al., 2012; Kulmala
70 et al., 2013; Lehtipalo et al., 2009, 2010, 2011; Yu et al., 2014a, b). China is suffering from severe
71 atmospheric particulate matter pollution in recent years (Chan and Yao, 2008; Yue et al., 2011). To
72 the best of our knowledge, only two studies were conducted in China to measure the occurrence of
73 new particles down to ~1 nm. In these two studies, air ions (Herrmann et al., 2014) or neutral
74 particles (Xiao et al., 2015) were measured by AIS or PSM in two urban locations of Yangtze River
75 Delta region. Both studies were conducted in the winter season.

76 Here we reported the nucleation and growth of sub-3 nm particles in the urban atmosphere of
77 Nanjing, China on arbitrarily selected observation days in spring, summer and winter of 2014-2015.
78 Our aim was to (1) provide new information about the initial steps of NPF based on size- and time
79 resolved nucleation rate and growth rate measurements, and (2) find possible limiting factors behind
80 the seasonal and diurnal variations of nucleation events in the polluted urban atmosphere.

81 **2. Methodology**

82 **2.1 Field measurements**

83 Nanjing is the second largest megacity after Shanghai in the Yangtze River Delta (YRD) region
84 of China (Chan and Yao, 2008). The YRD city cluster, covering 2.1×10^5 km² land with 170 million
85 residents, is one of the most populated and industrialized regions in China. Field measurement was
86 conducted from the third floor (15m above the ground level) of an academic building beside a
87 Chinese national meteorology observatory facility in NUIST campus (32.20° N, 118.71° E, symbol
88 ① in Figure 1). The sampling was carried out during the months of May (May 10-30, 2014), June

89 (June 1-15, 2014), December (December 24-31, 2014), February (February 16-22, 2015), and March
90 (March 1-7, 2015). Total 58 measurement days were arbitrarily selected to represent spring, early
91 summer and winter seasons, but to avoid any rain-event.

92 As part of an intensive summer campaign (12 August-12 September 2014), the summer
93 measurement was conducted at a local governmental meteorology observatory platform (32.06°N,
94 118.70°E) that is 14km south to the NUIST site (② in Figure 1). The instruments were housed in an
95 air conditioned trailer, using exactly the same sampling inlets as the NUIST site. The main aim of the
96 summer campaign was to understand the effects of regional emission control measures during the
97 2014 Young Olympic Games (August 1-September 15) on air quality. Because the two sites locate
98 within the same urban air shed, the measurement provided an opportunity to study seasonal variation
99 of nucleation and its relationship with meteorological variables and gaseous precursors.

100 Sub-3 nm clusters/particles (hereafter referred as particles) were measured with a nano
101 condensation nucleus counter system (nCNC) consisting of a Particle Size Magnifier (PSM model
102 A10, Airmodus Oy, Finland) and a butanol Condensation Particle Counter (model A20, Airmodus
103 Oy, Finland). During the measurement, an ambient air flow of 14 standard liters per minute (slpm)
104 was drawn into building room or trailer via a 72 cm long and 1.0 cm I.D diameter stainless steel (SS)
105 tube, which was extended outside the room/trailer horizontally. PSM then sampled a split flow of 2.5
106 slpm via a SS T-union. The design of the inlet tubing (length and air flow rate) was to minimize the
107 transport loss of nano particles. The size dependent transport survival ratios of sub-3 nm particles in
108 the inlet tubing was estimated (67 %-86 % for 1.4-3.0 nm) and corrected using a particle loss
109 calculator tool (von der Weiden et al., 2009).

110 PSM was operated in a continuous scanning mode with a cycle of 240 steps between saturator

111 flow rates of 0.1 and 1.0 slpm within 240 seconds. The particle cut-off sizes of the nCNC varied with
112 saturation ratios in the saturator (Vanhanen et al., 2011). A step-wise method was used to invert raw
113 scanning data to size spectrum (time resolution: 4 minutes) of sub-3 nm particles, which were
114 classified evenly into 6 size bins, i.e. 1.4-1.6, 1.6-1.9, 1.9-2.2, 2.2-2.4, 2.4-2.7, and 2.7-3.0 nm. The
115 inverted particle number concentrations in the 6 bins were referred as $N_{1.5}$, $N_{1.8}$, $N_{2.0}$, $N_{2.3}$, $N_{2.6}$ and
116 $N_{2.8}$, using mean values of upper and lower size boundaries in each bin. The step-wise method was
117 described in detail by Lehtipalo et al. (2014).

118 Particle size distributions in the range from 3 - 750 nm were obtained by integrating two
119 scanning mobility particle spectrometers (SMPS) with a nano-SMPS (a TSI differential mobility
120 analyzer DMA3085 and a condensation particle counter CPC3776; scanning range: 3 - 64 nm) and a
121 long-SMPS (TSI DMA3081 and CPC3775; scanning range: 64 - 750 nm). During the summer
122 campaign, only the long-SMPS was operated to scan particles from 8 - 350 nm. Scanning cycles of
123 both SMPS systems were 4 minutes, in order to synchronize with the nCNC. The SMPSs sampled
124 ambient air from a separate sampling inlet. The inlet was a 129 cm long and 1.0 cm I.D
125 horizontally-oriented SS tube with an air flow of 14 slpm. The transport loss of particles in the SMPS
126 inlets was corrected using size dependent survival ratios of 85-100% for particles > 3 nm.

127 Sulfur dioxide (SO₂), ozone (O₃), carbon monoxide (CO) and nitrogen oxides (NO and NO₂)
128 concentrations were measured every 1 minute with Thermo Environmental Instruments (model
129 43i-TLE, 49i, 48i, and 42i, respectively). When gaseous SO₂, O₃, NO₂ and CO data were not
130 available, hourly SO₂, O₃, NO₂ and CO were obtained from nearby local Environmental Protection
131 Agency (EPA) monitoring station. PM_{2.5} was monitored with Thermo Scientific TEOM 1405.
132 Meteorological variables including wind speed, wind direction, relative humidity (RH), temperature

133 and solar radiation flux were recorded every 1 hour during the measurement periods. Mean
134 concentrations of PM_{2.5}, SO₂, and O₃ were 79 μ g m⁻³, 10 ppbv and 48 ppbv, respective, during the
135 whole measurement period. Therefore, we regard our measurement environment as a polluted urban
136 atmosphere.

137

138 **2.2 Nucleation event and growth patterns**

139 A criterion was set to determine whether the nCNC detected sub-3nm particles in the atmosphere.
140 The criterion was that total particle concentration reading followed the supersaturation scanning
141 cycle of PSM so that the highest concentrations were measured at lowest cut-off sizes (see also
142 Figure 2 in Lehtipalo et al., 2014). However, it was possible in the step-wise inversion method that
143 the number concentration fluctuation of > 3 nm particles within a 4-min scanning cycle was wrongly
144 inverted to sub-3 nm particles even when sub-3 nm particles actually did not exist according to the
145 above criterion. As a result, the step-wise inversion method always reported a background sub-3 nm
146 particle concentration (N_{sub-3} , i.e. the sum of $N_{1.5}$, $N_{1.8}$, $N_{2.0}$, $N_{2.3}$, $N_{2.6}$ and $N_{2.8}$) of $0.5 \times 10^3 - 2 \times 10^3$
147 cm⁻³ in the nighttime and $3 \times 10^3 - 8 \times 10^3$ cm⁻³ in the daytime. Similar background levels of sub-3 nm
148 particles during non-NPF periods were also reported by other studies that used the nCNC (Kulmala
149 et al., 2013; Lehtipalo et al., 2014; Xiao et al., 2015). Following their procedures, we did not attempt
150 to subtract this background from N_{sub-3} reported in this study.

151 We defined sub-3 nm particle event as sub-3 nm particle occurrence in the atmosphere for which
152 the above criterion was fulfilled and furthermore N_{sub-3} higher than background level persisted for
153 longer than 1 h. In this study, we used sub-3 nm particle event as an approximate measure of
154 nucleation event. This is because (1) there was an approximately positive linear correlation between

155 N_{sub-3} and nucleation rate ($J_{1.4}$ in this study, see next section) with R^2 of 0.94 (Figure 2), and (2) N_{sub-3}
156 calculation needs only nCNC scanning data and was thus more readily available than $J_{1.4}$ calculation
157 which needs both nCNC and SMPS scanning data. Similar definition has been discussed in our
158 previous studies (Yu et al., 2014a, b). Apparently, a sub-3 nm particle event did not necessarily lead
159 to an NPF event always, but it indicated the intensity and frequency of nucleation in the atmosphere.
160 One focus in this work was to investigate the characteristics of sub-3 nm particle event.

161 Particle growth after nucleation is crucial to determine if nucleated particles could grow to
162 CCN-active sizes. We identified two growth patterns according to size spectrum characteristics in
163 sub-3 nm size range (Figure 3). In a Type A event (Figure 3a or b), size distribution $n(D_p, t)$ was
164 higher at smaller sizes (e.g., 1.4–1.6 nm) than $n(D_p, t)$ at larger sizes (e.g., 2.7–3.0 nm). The size
165 spectrum below 3 nm thus looked like a “volcano”. In a Type B event (Figure 3c or d), $n(D_p, t)$ was
166 lower at smaller sizes than $n(D_p, t)$ at larger sizes (“up-side-down volcano”). For the size range > 3
167 nm, depending on whether a banana-shape growth was seen, we further defined Type A1/A2 and
168 Type B1/B2 events: particles eventually grew to CCN-active sizes in Type A1 and B1 events, while
169 in Type A2 and B2 events banana-shape particle growth to CCN-active sizes was not seen. Therefore,
170 Type A1 and B1 events were equivalent to conventional NPF events based on either DMPS or SMPS
171 measurements.

172 Type B size distribution was more unusual since $n(D_p, t)$ of small particles were less than $n(D_p, t)$
173 of large particles in the sub-3 nm size range. We excluded the possibility of deteriorated nCNC
174 detection efficiencies for small particles due to high particle loading in the sample air. This is
175 because total number concentrations of nCNC during our measurements never approached nCNC
176 upper concentration limit $4 \times 10^5 \text{ cm}^{-3}$, especially in the early stage of nucleation when total particle

177 concentration was rather low. Our nCNC was also calibrated periodically using H₂SO₄-H₂O particles
178 in a laboratory flow tube to ensure the detection efficiency of the nCNC. Chemical composition
179 could be another factor of varying detection efficiencies. It is well known that organic substances
180 activate less readily in diethylene glycol (e.g. Kangasluoma et al. 2014). However, it is accepted in
181 general that new particles at larger sizes have higher mass fraction of organics than those at smaller
182 sizes in a NPF process. If organic substances activate less readily in DEG, the particles in larger bins
183 should have even lower detection efficiencies than smaller bins. Therefore, the increasing $n(D_p)$ with
184 D_p (i.e. upside down volcano) could not be simply due to lower detection efficiency of organic
185 substances.

186 **2.3 Formation rate and growth rate calculations with a simplified GDE method**

187 Conventional appearance time method determined growth rates (hereafter, GR) during the initial
188 period of NPF by finding the time steps when newly-formed particles appeared at certain size bins
189 and calculating the GR from the time differences between successive size bins (Kulmala et al., 2012;
190 Lehtipalo et al., 2014). This method was often not applicable to the NPF event with high GR below 3
191 nm, e.g., 0.3 nm/4 min (i.e. 4.5 nm h⁻¹) with size intervals 0.3 nm and scanning time intervals 4
192 minutes in our measurements. Furthermore, sub-3 nm particles were often generated persistently
193 throughout the daytime period. Maximum concentrations in the sub-3 nm size bins could appear
194 around noontime, which is a few hours later than the onset of nucleation. Therefore, we were not
195 able to pinpoint correctly maximum or 50% maximum concentrations at the onset of nucleation.

196 The rapid growth of small particles in the urban atmosphere was the motivation that we used an
197 alternative method to calculate growth rate and formation rate. Here, we analyzed 8 events (listed in
198 Table 1, including both Type A1/A2 and B1/B2 events) in detail, for which complete size spectra

199 from 1.4 - 750 nm were available without distorted, broken or noisy data. Total 8 size bins were
 200 classified: 6 evenly-divided size bins in sub-3 nm and 2 size bins in 3-30 nm (3-10 and 10-30 nm).
 201 For an aerosol population that is growing through simultaneous condensation and coagulation,
 202 aerosol general dynamic equation (GDE) describes the evolution of number concentration in a size
 203 bin between particle diameters D_{p1} and D_{p2} ($D_{p2} > D_{p1}$) as:

$$204 \frac{dN(D_{p1}, D_{p2}, t)}{dt} = J(D_{p1}, t) - J(D_{p2}, t) - \text{CoagSnk}(D_{p1}, D_{p2}, t) + \text{CoagSrc}(D_{p1}, D_{p2}, t) \quad (1)$$

205
 206 where $N(D_{p1}, D_{p2}, t)$ is the number concentration from D_{p1} to D_{p2} , inverted from nCNC or SMPS
 207 scanning data. $\text{CoagSnk}(D_{p1}, D_{p2}, t)$ and $\text{CoagSrc}(D_{p1}, D_{p2}, t)$ are the sink term defining the
 208 coagulation removal of particles and the source term defining the coagulation production of particles.
 209 J is condensational growth flux (i.e. particle formation rate) across the lower (D_{p1}) or upper (D_{p2})
 210 boundaries of a size bin. In the first size bin of 1.4-1.6 nm, $J(1.4 \text{ nm}, t)$, or simply $J_{1.4}$, is the
 211 unknown formation rate of the smallest particles that we measured.

212 The GDE here was the same as the Eq. 1 by Kuang et al. (2012). In their method, gaseous H_2SO_4
 213 was measured simultaneously and a constant $GR(D_p, t) / GR_{\text{H}_2\text{SO}_4}(D_p, t)$ ratio at a given size over time
 214 was assumed. Their $GR(D_p, t)$ was then solved by fitting the GDE to the measured size distributions.
 215 In our study, however, we did not measure gaseous H_2SO_4 . Instead, $J(30 \text{ nm}, t)$ in the largest size
 216 bin, which is the condensational growth flux out of 30 nm, was set to zero. This simplification was
 217 valid in the four Type A2/B2 events when particles never grew to > 30 nm (March 4, February 19,
 218 May 20 and May 16). In the rest four Type A1/B1 events (February 18, December 27, May 15, and
 219 August 15), this was also valid during the early NPF period when particles did not grow out of 30 nm
 220 and during the late NPF period when particles grew out of 30 nm completely. During the middle

221 period of events (usually around 11:00 AM-14:00 PM), $J(30 \text{ nm}, t)$ was underestimated and thus
222 $J_{1.4}$ could be regarded as a lower estimate. In the four Type A2/B2 events, our calculation showed
223 that J_{10} was only 0-4% of $J_{1.4}$. Xiao et al. (2015) and Kulmala et al. (2013) measured both $J_{1.5}$ and J_3
224 using appearance time method. Their J_3 was less than 7% of $J_{1.5}$. Furthermore, $J_{30}/J_{1.4}$ ratio should be
225 even smaller than $J_{10}/J_{1.4}$ or $J_3/J_{1.5}$ ratios, considering the 8 events were carefully selected to ensure
226 all sub-30 nm particles were grown from nucleation (not emitted directly from emission sources like
227 vehicular engine). All these evidences supported that even if J_{30} was set to 0, $J_{1.4}$ would not be
228 underestimated more than 7% when particles grew cross 30 nm on February 18, December 27, May
229 15, and August 15.

230 Equation 1 requires the convergence of condensational growth (J), coagulation terms (CoagSnk
231 and CoagSrc) and the changing rate of particle number concentration (dN/dt). Using Eq. 1 we can
232 therefore calculate the nucleation rate $J(1.4 \text{ nm}, t)$ and formation rates $J(D_p, t)$ across all size bin
233 boundaries from 1.6 to 10 nm. After the formation rates $J(D_p, t)$ were obtained, $GR(D_p, t)$ was
234 calculated from $J(D_p, t)/n(D_p, t)$, where $n(D_p, t)$ is size distribution calculated as $n(D_p, t) = \frac{dN(t)}{dD_p}$
235 for each size bin. On the other hand, the appearance time method could still be applied to (1) the size
236 range of $> 3 \text{ nm}$ where size intervals were large (2-6 nm), and (2) the size range of $< 3 \text{ nm}$ when GR
237 was small. The results from appearance time method will also be showed in the next section.

238

239 3. Results and discussion

240 Section 3.1, sections 3.2-3.4 and section 3.5 were organized, respectively, to address the
241 following 3 issues: (1) seasonal variation, diurnal variation and limiting factors of nucleation event
242 (represented by sub-3 nm particle event) in the polluted urban atmosphere, (2) time- and size

243 dependent nucleation rate and growth rate of sub-3 nm particles, and their implications for nucleation
244 and growth mechanisms, (3) Inhibited particle growth to CCN-active sizes in strong nucleation
245 events of Type B2.

246 **3.1 Seasonal and diurnal variations of nucleation event**

247 As seen from Figure 2, there was an approximate linear correlation between N_{sub-3} and $J_{1.4}$ with
248 the slope of $N_{sub-3}/J_{1.4}$ equal to ~ 160 . This seemed to suggest that the average residence time of
249 new particles in the sub-3 nm size range was 160 seconds before they were scavenged due to
250 coagulation or grew out of 3 nm. The sub-3 nm particles observed at the present work were thus
251 formed in situ in the urban atmosphere and not likely to be carried-over by air transport. In this
252 section we used sub-3 nm particle event as an approximate measure of nucleation.

253 We observed significant seasonal characteristics of nucleation event (Figure 4). Nucleation was
254 rare and weak in summer, while it was commonly observed in all other seasons. During our
255 measurements from 2014 to 2015, nucleation events occurred on 81% of all spring observation days
256 (May 2014), 53% in early summer (June 2014), 10% in summer (August and September 2014), and
257 64% in winter (December 2014, February and March 2015). We compared intensity (N_{sub-3}) and
258 frequency of nucleation events, as well as meteorological variables (temperature, RH, wind speed,
259 and solar radiation flux) and gaseous pollutants (SO_2 , NO_2 , CO and O_3) for spring, summer and
260 winter seasons. June was not shown in Figure 4 for comparison, because it was a transit season from
261 spring (May) to summer (August and September). The data were first averaged over the entire event
262 period for each event; and we then used event-averaged data to create box and whistler plots for the 3
263 seasons. $PM_{2.5}$ was used here as a surrogate of condensational sink (CS), because of the more ready
264 availability of $PM_{2.5}$ data than SMPS data.

265 As shown in Figure 4, nucleation in summer was characterized by lowest frequency, lowest
266 N_{sub-3} ($2.2 \times 10^4 \text{ cm}^{-3}$), and short nucleation period (only 1-2 hours). Strict emission control measures
267 during the 2014 Youth Olympic Games resulted in relatively low $\text{PM}_{2.5}$ level ($32 \pm 8 \mu \text{g m}^{-3}$),
268 which should favor nucleation. However, relatively low SO_2 concentration ($1.4 \pm 0.6 \text{ ppbv}$), high
269 temperature ($26 \pm 2 \text{ }^\circ\text{C}$), and high RH ($74.3 \pm 4.2 \%$) might not be in favor of nucleation. A simple
270 H_2SO_4 proxy ($\text{Radiation} \times \text{SO}_2 / \text{PM}_{2.5}$) indicated that summer H_2SO_4 concentration was likely to be the
271 lowest among the 3 seasons, which could explain low nucleation intensity/frequency.

272 We further examined diurnal variations of N_{sub-3} and other variables on event and non-event days
273 in winter (Figure 5). Because nucleation in winter was characterized by Type B event
274 (“up-side-down volcano” below 3 nm), event days were further divided to Type B1 and Type B2
275 events depending on whether banana-shape particle growth was seen. The difference between Type
276 B1 and B2 will be discussed later in Section 3.5. During the non-event days, N_{sub-3} ranged from
277 $2.4 \times 10^3 \text{ cm}^{-3}$ in the night to 8.0×10^3 in the day, which was close to background levels. During the
278 event days, N_{sub-3} in the night was close to that of non-event days, but could reach $8 \times 10^4 - 20 \times 10^4$
279 cm^{-3} in the middle of the day. This was more than 10 times higher than those on the non-event days.
280 From Figure 5 we can see that non-event day had higher concentrations of anthropogenic precursors
281 (indicated by SO_2 , NO_2 , and CO), but nucleation seemed to be limited by higher pre-existing particle
282 surface area (indicated by $\text{PM}_{2.5}$), higher temperature and RH, and lower radiation flux.
283 Photochemistry indicators O_3 was also lower during non-event days.

284 Nucleation in spring was characterized by highest frequency (81%) among all seasons. Highest
285 gaseous pollutant concentration of (H_2SO_4 proxy, SO_2 , NO_2 , CO and O_3) and radiation seemed to the
286 favorable factors to explain this. However, N_{sub-3} in spring ($3.3 \times 10^4 \text{ cm}^{-3}$) was much lower than that

287 in winter ($11.2 \times 10^4 \text{ cm}^{-3}$). Unfavorable factors included high pre-existing particle surface area ($\text{PM}_{2.5}$:
288 $112 \pm 68 \mu \text{ g m}^{-3}$) and high temperature ($27 \pm 4 \text{ }^\circ\text{C}$) in spring. Integrating the above seasonal and
289 diurnal variation information in Figure 4 and Figure 5, we tentatively identified that the limiting
290 factors for nucleation in our urban atmosphere were (1) radiation, temperature, RH and CS in winter
291 and spring, and (2) temperature, RH and available gaseous precursors in summer.

292 Out of total 90 measurement days, March 4, 2015 in winter was the only day that we observed
293 significant nocturnal nucleation. Sunrise and sunset were at 6:29 AM and 18:00 PM local time on
294 March 4, but nucleation were observed persistently from 4:00 AM - 20:00 PM. $N_{\text{sub-3}}$ increased from
295 $3.5 \times 10^3 \text{ cm}^{-3}$ at 4:00 AM to $6.3 \times 10^4 \text{ cm}^{-3}$ before sunrise. During 10:00-11:00 AM, peak $N_{\text{sub-3}}$
296 reached $3 \times 10^4 \text{ cm}^{-3}$, 3 times higher than the average of all other event days in winter. Apparently,
297 nocturnal nucleation on March 4 could not be explained as carry-over of daytime particles nor being
298 associated with photochemistry. This implied the existence of certain dark nucleation source. There
299 are a number of observations that have also shown nighttime particle formation events in various
300 atmospheric conditions (Junninen et al., 2008; Lehtipalo et al., 2011; Lee et al., 2008; Ortega et al.,
301 2009, 2012; Russell et al., 2007; Suni et al., 2008; Svenningsson et al., 2008; Yu et al., 2014), but the
302 mechanisms behind the nocturnal nucleation are yet still highly speculative. With our instrument
303 capability in this work, we could not deduce any valuable information on the nocturnal nucleation
304 mechanism, except that we found the air mass on 04 March was relatively clean (both CS and gases,
305 mean CS: 0.15 s^{-1}), and temperature and RH (mean: 4.4°C and 33%) were favorable for nucleation.

306

307 **3.2 Size- and time dependent formation rates of sub-3 nm particles**

308 We observed 23 Type A events and 9 Type B events during the measurements. The different size

309 distribution patterns (Figure 3) were probably linked to the mechanism or intensity of nucleation and
310 growth. To address this issue, we first compared the formation rates and growth rates in two types of
311 events. Formation rates J of 1.4, 1.6, 1.9, 2.2, 2.4, 2.7 and 3.0 nm particles were shown in Figure 6
312 (upper panels) for typical Type A and Type B events. It is obvious that $J_{1.4}$ was much higher on
313 February 18 (Type B) than that on May 15 (Type A). A clear time dependence of J was observed. For
314 example, $J_{1.4}$ was $60 \text{ cm}^{-3} \text{ s}^{-1}$ at the onset of the nucleation event on May 15 and increased to 300
315 $\text{cm}^{-3} \text{ s}^{-1}$ in the middle of the day. In the type B event on February 19, the initial and peak $J_{1.4}$ were
316 2.1×10^2 and $1.2 \times 10^3 \text{ cm}^{-3} \text{ s}^{-1}$ respectively. Therefore, our method provided more information of
317 nucleation than conventional calculation methods that usually showed only an averaged J at the onset
318 of a nucleation event. Our method was also different from Kulmala et al. (2013). Their
319 time-dependent formation rate on an event day was equal to size distribution $n(D_p, t)$ times a constant
320 growth rate at the onset of the event obtained with the appearance time method.

321 The diurnal variation of J implied that nucleation was probably linked to sunlight induced
322 photochemistry. We calculated the correlations between $J_{1.4}$ and an H_2SO_4 proxy for the 8 events of
323 our interest. The H_2SO_4 proxy was calculated following $[\text{H}_2\text{SO}_4] = 8.21 \times 10^{-3} k \cdot \text{Radiation} \cdot$
324 $[\text{SO}_2]^{0.62} \cdot (\text{CS} \cdot \text{RH})^{-0.13}$ (Eq. 8 of Mikkonen et al. 2011), where k is the temperature-dependent
325 reaction-rate constant. Figure 7a show that good linear correlation was usually seen for every single
326 event with R^2 ranging from 0.72 to 0.86 for 6 out of 8 events. A moderate R^2 of 0.56 was obtained for
327 August 15. R^2 was lowest (0.34) on March 4, 2015. This is not surprising because we know March 4
328 was the only day with nocturnal nucleation during the measurement period. The slopes of $\log J_{1.4}$ vs.
329 $\log [\text{H}_2\text{SO}_4]$ were close to 1 in all events (0.82-1.17, excluding March 4), indicating activation theory
330 can explain the nucleation mechanism in our urban atmosphere.

331 If data points of all the 8 events were put together, the linear correlation between H₂SO₄ proxy
332 and $J_{1.4}$ deteriorated (slope=1.1, $R^2=0.17$, Figure 7b). In spite of considerable scattering, most of data
333 points located between $J_{1.4}=10^{-4.1} \times [\text{H}_2\text{SO}_4]$ and $J_{1.4}=10^{-6.3} \times [\text{H}_2\text{SO}_4]$. An interesting finding is that
334 the scattering of $J_{1.4}$ vs. [H₂SO₄] proxy among all 8 events was probably due to temperature or season
335 change (Figure 7b). More specifically, with the same level of H₂SO₄ proxy, $J_{1.4}$ was higher in winter
336 with lower temperature than in spring/summer with higher temperature. There were two possibilities
337 behind the deteriorated linear correlation between H₂SO₄ proxy and $J_{1.4}$: (1) inaccurate H₂SO₄ proxy
338 and (2) other varying factors in nucleation mechanism. First, it was very likely that H₂SO₄
339 concentrations in our polluted urban atmosphere were overestimated by the H₂SO₄ proxy of
340 Mikkonen et al. (2011), which was based on statistic regression of historical datasets from relatively
341 clean Europe/USA atmosphere. The extent of overestimation may vary with the levels of predictor
342 variables (e.g., SO₂, temperature, CS). Mean SO₂ mixing ratios were 10.5 and 7.3 ppbv in
343 spring/summer and winter during our measurements, respectively. These were 1 order of magnitude
344 higher than SO₂ mixing ratios at the 6 European and USA sites (mean values: 0.23-3.4 ppbv,
345 Mikkonen et al., 2011). Our CS in the 8 events was on the order of magnitude of 10⁻² s⁻¹, again higher
346 than 10⁻³ s⁻¹ in Mikkonen et al. (2011). Mikkonen et al. (2011) had already pointed out that the
347 predictive ability was lower for long term data due to atmospheric condition changes in different
348 seasons.

349 Second, organic condensing vapor concentrations in particle growth events were higher in winter
350 than those in spring/summer (Table 1, see Section 3.4). If the organics were also involved in
351 nucleation, $J_{1.4}$ should be enhanced in winter. The enhancement of nucleation by organics (most
352 likely anthropogenic organics in our urban atmosphere) could be supported by the comparison of $J_{1.4}$

353 dependences on H_2SO_4 between our study and the measurements in the Boreal forest: besides
354 possible H_2SO_4 overestimation, $J_{1.4}=10^{-4.1} \times [\text{H}_2\text{SO}_4] - 10^{-6.3} \times [\text{H}_2\text{SO}_4]$ in our sites was much higher
355 than $J_{1.5}=1.06 \times 10^{-7} [\text{H}_2\text{SO}_4]^{1.1}$ in Hyytiälä during active aerosol formation periods (Kulmala et al.,
356 2013). At last, low temperature itself might enhance nucleation in winter (Brus et al., 2011) via
357 increasing the saturation ratios of all nucleation precursors (e.g., water, H_2SO_4 , organics).

358 359 **3.3 Size- and time dependent growth rates of sub-3 nm particles**

360 Particle size distribution $n(D_p)$ and corresponding $GR(D_p)$ at an instant in time during the events
361 were shown in Figure 6 middle and lower panels. A local minimum of $n(D_p)$ at 2.4 nm, followed by a
362 local maximum somewhere between 2.5 and 10 nm, was seen on May 15, 2014. Such size
363 distribution characteristics on May 15, 2014, as well as on all other Type A event days, was also
364 observed by Kulmala et al. (2013) in the Boreal forest (Figure 1A and S9A in their paper) and by
365 Jiang et al. (2011b) in the urban area of Atlanta, USA (Figure 1 in their paper). We further examined
366 the growth rates in the size range of 1-3 nm on May 15, 2014. It was shown that there was a local
367 maximum of $GR(D_p)$ at 2.4 nm. This could explain why $n(D_p)$ was increasing in 2.4-3 nm size range:
368 when particle condensational flow out of a size bin was slowed down, it was possible that particles
369 flowing into the size bin accumulated, leading to particle number increase in the bin.

370 We saw more unusual behaviors of $n(D_p)$ and $GR(D_p)$ in the Type B event on February 18
371 (Figure 6 right panels): $GR(D_p)$ decreased monotonically in the size range of 1.4 - 3 nm, and
372 accordingly $n(D_p)$ increased monotonically at the same time. A high $GR(D_p)$ of 25 nm h^{-1} was
373 observed at 1.6 nm and $GR(D_p)$ decreased rapidly to 1.7 nm h^{-1} at $\sim 3 \text{ nm}$. If we consider that $GR(D_p)$
374 below 1.6 nm would eventually decrease due to strong Kelvin effect of all possible precursors

375 (H₂SO₄ or organics), the overall trend of $GR(D_p)$ in the Type B event was in fact the same as Type A:
376 for the smallest clusters, growth rate was small (possibly below 1 nm h⁻¹) and increased with D_p . It
377 reached a local maximum somewhere between 1-3 nm, after which $GR(D_p)$ decreased with D_p . For a
378 typical NPF event, $GR(D_p)$ would eventually increase again after a local minimum between 3-10 nm.
379 The difference between the Type A event (February 18) and Type B event (May 15) was the D_p of
380 local maximum $GR(D_p)$ (2.4 nm vs. 1.6 nm).

381 The interesting behaviors of $n(D_p)$ and $GR(D_p)$ in our urban atmosphere were different from the
382 stereotyped understanding that steady-state cluster size distribution $n(D_p)$ decreases with D_p in
383 nucleation and GR increases monotonically with D_p in an NPF event. It should be pointed out that if
384 we calculated the overall GR in 1.4-3 nm, $GR_{1.4-3}$ was 3.6 nm h⁻¹ on May 15 and 4.4 nm h⁻¹ on
385 February 18, which were still smaller than GR_{3-20} during the initial period of the events (7.7 and 6.0
386 nm h⁻¹, calculated using appearance time method). Table 1 showed that a faster GR_{3-20} than $GR_{1.4-3}$
387 were quite common, except in two events on May 16 and 20 when particles did not grow beyond 3
388 nm. Overall, GR was still increasing with increasing D_p .

389 Kuang et al. (2012) had also reported a local maximum of GR at ~2.6 nm in an NPF event
390 measured in Atlanta, USA (Figure 1b in their paper). In this study we further point out that GR could
391 decrease monotonically with D_p in 1-3 nm range in strong nucleation events. Our GR was calculated
392 from a simplified GDE method, however, the decrease of GR in 1-3 nm size range could be easily
393 inferred from the size spectra shown in Figure 3 or Figure 6 middle panels: for a D_{p2} that was larger
394 than D_{p1} , particle formation rate $J(D_{p2})$ must be smaller than $J(D_{p1})$. If we observed a higher $n(D_{p2})$
395 than $n(D_{p1})$, $GR(D_p)$ that was equal to $J(D_p)/n(D_p)$ must be smaller at D_{p2} than D_{p1} .

396 Apparently, the complicated growth rate behaviors in our polluted urban atmosphere can not be

397 explained by H₂SO₄ condensation alone, not only because H₂SO₄ condensational growth rate
398 ($GR_{H_2SO_4}$, calculated from the H₂SO₄ proxy and shown as black dashed lines in Figure 6) was smaller
399 than the measured growth rate ($GR_{measured}$), but also because $GR_{H_2SO_4}$ curve should follow a
400 monotonically decreasing trend in > 1 nm sizes assuming a collision-only condensational growth
401 without vaporization (Nieminen et al., 2010).

402

403 **3.4 Growth rate due to activating vapor on newly formed nuclei in sub-3 nm sizes**

404 Kulmala et al. (2013) has attributed the increasing $n(D_p)$ with D_p at 1.7-2.0 nm to particle
405 activation by organic vapors using nano-Köhler theory. The theory (Anttila et al., 2004; Kulmala et
406 al., 2004a,b) suggested that an activating organic vapor was dissolved in newly formed inorganic
407 nuclei at certain size between 1-3 nm. Equilibrium organic vapor pressure over the inorganic nuclei
408 $C_{surface}$ was thus lowered. However, the theory was usually used to describe how the GR of 1-3 nm
409 particles was enhanced by organic vapors. Attention has never been paid to the decreasing of GR
410 after local maximum.

411 Here, we continued our discussion based on the nano-Köhler theory to provide an explanation of
412 GR behaviors observed in our urban atmosphere. The net uptake of gaseous molecules by a
413 nanoparticle was driven by the difference of the condensational flux (governed by gas-phase
414 concentration far from the particle C_∞) and the evaporation flux (governed by volatility). If the
415 particle was well mixed, the volatility was directly related to $C_{surface}$, which was determined by the
416 pure component saturation vapor pressure C^* , particle curvature $\exp\left(\frac{4\sigma v}{kTD_p}\right)$ and particle composi-
417 tion. The growth rate due to an activating organic vapor (hereafter, denoted as ELVOC, extremely
418 low volatility organic compound) was expressed as

419
$$GR_{ELVOC} = \frac{\gamma}{2\rho_v} \left(1 + \frac{D_v}{D_p}\right)^2 \left(\frac{8kT}{\pi}\right)^{\frac{1}{2}} \left(\frac{1}{m_p} + \frac{1}{m_v}\right)^{\frac{1}{2}} m_v (C_\infty - C_{\text{surface}}) \quad (2)$$

420 where $C_{\text{surface}} = C^* \exp\left(\frac{4\sigma v}{kTD_p}\right) (x_{D_p} + \exp(-\varphi(D_p/D_{p0})^3))$.

421 The kinetic prefactor $\frac{\gamma}{2\rho_v} \left(1 + \frac{D_v}{D_p}\right)^2 \left(\frac{8kT}{\pi}\right)^{\frac{1}{2}} \left(\frac{1}{m_p} + \frac{1}{m_v}\right)^{\frac{1}{2}} m_v$ was taken from Nieminen et al.
 422 (2010). x_{D_p} was the mole fraction of water-soluble ELVOC in the pseudobinary solution consisting
 423 of ELVOC and an aqueous-phase sulfate nuclei. The nuclei diameter was the D_p with local
 424 maximum GR (activation diameter, $D_{p,act}$). The pseudobinary solution was treated ideal in the Eq. 2.
 425 For $D_p > D_{p,act}$, the dilution of this pseudobinary solution made C_{surface} increase to merge with
 426 Kelvin equilibrium curve (Figure 1 in Kulmala et al. 2004a). For $D_p < D_{p,act}$, the condensation of the
 427 ELVOC was in effect dominated by heterogeneous nucleation onto insoluble nuclei. Therefore,
 428 C_{surface} at D_p smaller than $D_{p,act}$ should also increase to merge with Kelvin equilibrium curve. To
 429 account for this effect, an empirical term $\exp(-\varphi(D_p/D_{p0})^3)$ was added to Eq. 2. Here, D_{p0} was 1
 430 nm to cancel off the unit of D_p . If $D_p \rightarrow 0$, the term $\rightarrow 1$. If $D_p \rightarrow D_{p,act}$, the term $\rightarrow 0$. Consequently,
 431 $C_\infty - C_{\text{surface}}$ had a local maximum at the $D_{p,act}$. On even larger particles >10 nm, $C_\infty - C_{\text{surface}}$
 432 would eventually increase due to weakened Kelvin effect. Therefore, the trend of $C_\infty -$
 433 C_{surface} coincided with the change of GR with D_p .

434 We fitted GR_{ELVOC} with the measured GR in sub-3 nm sizes ($GR_{GDE\ method}$ in Figure 8) at an
 435 instant in time by adjusting 3 free parameters in Eq. 2: C^* , C_∞ , and φ . Other parameters like
 436 surface tension (0.02 N m^{-1}) and molar volume ($135.5 \text{ cm}^3 \text{ mol}^{-1}$) of ELVOC were taken from
 437 Kulmala et al. (2004a). Molecule diameter d_v (0.8 nm) and condensed-phase density ρ_v (1.5 g cm^{-3})
 438 of ELVOC were taken from Ehn et al. (2014). Uptake coefficient γ was calculated following
 439 Nieminen et al. (2010). The fitting results in Figure 8 showed that the dependence of $GR_{GDE\ method}$ on

440 D_p below 3 nm could be well reproduced by Eq. 2 for both Type A and Type B events. ϕ ranged
441 from 0.4-1.0 for the 8 events. Other 2 free parameters were shown in Table 1. The activating vapor
442 concentrations C_∞ were $2.3 \times 10^7 - 2.0 \times 10^8 \text{ cm}^{-3}$. The saturation vapor concentration C^* were
443 $2.5 \times 10^6 - 5.7 \times 10^7 \text{ cm}^{-3}$. They were within the orders of magnitude of $10^7 - 10^8 \text{ cm}^{-3}$ and $10^6 - 10^7 \text{ cm}^{-3}$
444 suggested by Kulmala et al. (2004a), respectively.

445 For comparison, the GR calculated from appearance time method was also shown in Figure 8
446 ($GR_{AT\ method}$) for > 3 nm particles on May 15, February 18 and February 19, as well as for sub-3 nm
447 particles on May 20 when particle growth was relatively slow. It can be seen that the GR on May 20
448 calculated from the two methods agreed well with each other, leading credit to our GDE method.
449 $GR_{AT\ method}$ in >10 nm sizes was usually underestimated by GR_{ELVOC} . This could be interpreted as
450 other condensing vapors with higher volatility may contribute to particle growth in the larger
451 particles. It should be noted that the appearance time method followed the time steps when
452 newly-formed particles appeared in successive size bins and thus $GR_{AT\ method}$ was not the growth rates
453 at the same instant in time.

454 For all the 8 nucleation events, Table 1 summarizes the measured values of overall growth rate
455 in 1.4-3 nm ($GR_{1.4-3}$), maximum growth rate in 1.4-3 nm ($GR_{max,1.4-3}$), overall growth rate in 3-20 nm
456 (GR_{3-20}), nucleation rate ($J_{1.4}$), activation diameter ($D_{p,act}$), CS , and temperature (T) during the event
457 periods with maximum nucleation rates. Corresponding estimates of Mikkonen H_2SO_4 proxy, C_∞
458 and C^* were shown in the right 3 columns. It can be seen that in comparison with more
459 conventional Type A events, Type B events usually occurred with (1) higher $J_{1.4}$, $GR_{max,1.4-3}$, $GR_{1.4-3}$,
460 C_∞ , and CS ; (2) smaller $D_{p,act}$; and (3) lower T . However, the H_2SO_4 proxy and GR_{3-20} were similar
461 in Type A and Type B events. Based on these estimations, we concluded that higher ELVOC

462 concentration C_{∞} was the key factor leading to the higher $J_{1.4}$ and $GR_{1.4-3}$, which in turn resulted in
463 the different size spectrum pattern in Type B events (“up-side-down volcano”) from in Type A
464 events (“volcano”).

465 It should be noted that the organic vapor concentrations C_{∞} referred to in this study were not
466 directly measured, but estimated based on Eq. (2). Aerosol dynamic processes, such as nucleation,
467 coagulation, and the condensation growth of H_2SO_4 and water vapors, were not considered explicitly
468 in Eq. (2). In addition, bulk thermodynamics was applied in Eq. (2) for extremely small
469 clusters/particles of sub-3 nm sizes. Therefore, although our calculation provided an possibility to
470 explain the size dependence of growth rate observed in the polluted urban atmosphere, C_{∞} in this
471 study was subject to uncertainties in (1) the growth rate derived from the GDE method, (2) the theory
472 by which the growth rate was related to the organic vapor concentration, and (3) H_2SO_4 level which
473 also contributed to the initial growth.

474

475 **3.5 Inhibited particle growth to CCN-active sizes in strong nucleation events of Type B2**

476 Type B2 was strong nucleation event that produced rather high concentrations of new particles
477 in sub-20 nm size range (Figure 3d). High concentrations of activating vapor in these events (e.g.,
478 C_{∞} : $1.4-2.0 \times 10^8 \text{ cm}^{-3}$ on February 18 and March 4) should favor a banana-shape NPF event with fast
479 growth of particles >20 nm, due to weakened Kelvin effect. However, it was puzzling to us why new
480 particles accumulated in 2-20 nm and did not grow further on Type B2 event days (see Figure 3d).
481 We first examined the air mass trajectory characteristics of Type B2 events. Compared with Type B1,
482 Type B2 was characterized by long range transport air masses from far north of China and Mongolia.
483 The lumped trajectories with insignificant wind direction change imply that the air mass in Type B2

484 event was quite uniform. In addition, meteorological and chemical variables (high solar radiation
485 flux and wind speed, low temperature, PM_{2.5}, SO₂, NO₂, CO and O₃, green lines in Figure 5)
486 collectively suggested that Type B2 was typical regional event in homogeneous cold air masses.
487 Therefore, the interrupted growth of new particles was not likely to be a result of wind direction
488 change.

489 As seen from Figure 5, meteorological variables on Type B2 days were generally more favorable
490 in aiding particle growth than on Type B1 days: lower PM_{2.5}, lower temperature, and higher solar
491 radiation flux. The unfavorable factors in Type B2 events, however, included lower concentrations of
492 SO₂, NO₂, and CO (anthropogenic emission indicators), lower secondary photochemical product
493 indicators O₃ and lower particle phase sulfate in 100-1000 nm (X. Ge, private communication, 2015,
494 X. Ge conducted simultaneous AMS measurement during our measurement periods). All these
495 evidences suggested that further particle growth in Type B2 events was limited by certain condensing
496 vapor other than ELVOC. Consequently, although there was a pool of sub-20 nm particles, they were
497 not further “activated” due to the low availability of this condensing vapor. Following the
498 terminology of Donahue et al. (2011, 2012), we called this condensing vapor LVOC (low volatility
499 organic compounds)

500 The above hypothesis was sound if we considered that the identity of LVOC for the growth of
501 particles > 20 nm could be different from ELVOC for sub-3 nm particle growth. Hirsikko et al. (2005)
502 observed that GR_{3-20} demonstrated an opposite seasonal cycle to $GR_{1.3-3}$: GR_{3-20} was higher in
503 summer, whereas $GR_{1.3-3}$ was higher in winter. This suggested that the condensing vapors were
504 different in identity for particles of different sizes. Hirsikko et al. (2005) attributed the condensing
505 vapors for GR_{3-20} to biogenetic VOCs. In our urban atmosphere, according to Figure 5, LVOC was

506 more likely to be from anthropogenic sources associated with SO₂, NO_x and CO emissions. A picture
507 of the growth process was thus like this: ELVOC of lower volatility, lower concentration and higher
508 water solubility activated inorganic nuclei and accelerated particle growth in smaller sizes. This in
509 turn assisted in the condensation of LVOC of high volatility, low solubility, but with larger amount
510 of mass. The further growth of particles >20 nm, which means significant increment of particle mass,
511 needed continuous supply of LVOC from the anthropogenic sources. On the Type B2 days, LVOC
512 supply was not adequate (low SO₂, CO and NO_x). As a result, continuous banana-shape particle
513 growth did not take place.

514 **4. Conclusion**

515 NPF can contribute to CCN only after going through nucleation, initial growth steps and
516 subsequent growth to CCN-active sizes. This study provided the evidences of limiting factors in
517 these processes in a polluted urban atmosphere in China. We observed atmospheric nucleation events
518 on 42 out of total 90 observation days, but particles could grow to CCN-active sizes on only 9 days,
519 which was equivalent to 9 conventional NPF events. In summer, strict emission control measures
520 during the 2014 Youth Olympic Games resulted in relatively low PM_{2.5} and anthropogenic trace
521 gases (SO₂, NO₂, CO and O₃) levels. Infrequent nucleation was thus limited by both low
522 concentrations of gaseous precursors and high temperature and RH in summer. In more polluted
523 winter and spring atmosphere, precursor supply was not limiting anymore; nucleation occurred once
524 meteorological conditions were favorable (i.e. low CS and temperature/RH, higher solar radiation).
525 However, for the further growth of sub-3 nm particles to CCN-active sizes, anthropogenic gaseous
526 precursors again became limiting factors.

527 A simplified GDE method was used in this study to calculate particle formation rates first and

528 then growth rates. Nucleation events were strong in the polluted urban atmosphere of Nanjing. Initial
529 $J_{1.4}$ at the onset and peak $J_{1.4}$ at the noontime could be up to $2.1 \times 10^2 \text{ cm}^{-3} \text{ s}^{-1}$ and $2.5 \times 10^3 \text{ cm}^{-3} \text{ s}^{-1}$,
530 respectively, during the 8 nucleation events selected from different seasons. The diurnal variation of
531 $J_{1.4}$ implied that nucleation was usually linked to sunlight induced photochemistry. Time-dependent
532 $J_{1.4}$ showed good linear correlations with the H_2SO_4 proxy for every single event, except a day with
533 significant nocturnal nucleation. However, the correlation between $J_{1.4}$ and the H_2SO_4 proxy for all 8
534 events deteriorated, which might reflect the effect of temperature or assisting vapor concentration in
535 the nucleation. The deteriorated correlation could also be due to the lower predictive ability of the
536 H_2SO_4 proxy in the polluted urban atmosphere for different seasons.

537 In all nucleation events, a local maximum growth rate was observed between 1-3 nm with GR up
538 to 25 nm h^{-1} . This means GR was not monotonically increasing with particle size. The overall $GR_{1.4-3}$,
539 however, was still smaller than GR_{3-20} , if particles could grow beyond 3 nm. The local maximum
540 growth rate was interpreted, using nano-Köhler theory, as the solvation effect of organic activating
541 vapor in newly formed inorganic nuclei. Based on our estimation, high ELVOC concentration of
542 $2.3 \times 10^7 - 2.0 \times 10^8 \text{ cm}^{-3}$ was expected to be the key factor leading to high $GR_{1.4-3}$. The varying GR of
543 new particle in turn resulted in the different particle growth patterns that we observed in Nanjing.

544 Our results call for a more robust proxy of gaseous H_2SO_4 to be developed for polluted urban
545 conditions. The study also brought up an urgent need for developing means to measure or estimate
546 activating organic vapor (i.e. ELVOC) levels in the initial growth steps of atmospheric NPF. Our
547 year-round measurement data provided valuable size evolution data of sub-3 nm clusters/particles to
548 evaluate previous aerosol dynamic models of new particle formation. A robust dynamic model was
549 needed to appropriately treat all aerosol and gas-phase processes in the initial growth steps.

550

551 **Acknowledgements**

552 This work was supported by National Science Foundation of China (41405116,
553 41275142, 41575122), Natural Science Foundation of Jiangsu Province (BK20140989), and Jiangsu
554 Specially Appointed Professor grant. The measurement campaigns were partially funded by the
555 Priority Academic Program Development of Jiangsu Higher Education Institutions (PAPD). We
556 thank Dr. Vijay P. Kanawade and Dr. Xinlei Ge for valuable discussion.

557

558 **References:**

559 Almeida, J., Schobesberger, S., Kurten, A., Ortega, I. K., Kupiainen-Maatta, O., Praplan, A. P.,
560 Adamov, A., Amorim, A., Bianchi, F., Breitenlechner, M., David, A., Dommen, J., Donahue, N.
561 M., Downard, A., Dunne, E., Duplissy, J., Ehrhart, S., Flagan, R. C., Franchin, A., Guida, R.,
562 Hakala, J., Hansel, A., Heinritzi, M., Henschel, H., Jokinen, T., Junninen, H., Kajos, M.,
563 Kangasluoma, J., Keskinen, H., Kupc, A., Kurten, T., Kvashin, A. N., Laaksonen, A., Lehtipalo,
564 K., Leiminger, M., Leppa, J., Loukonen, V., Makhmutov, V., Mathot, S., McGrath, M. J.,
565 Nieminen, T., Olenius, T., Onnela, A., Petaja, T., Riccobono, F., Riipinen, I., Rissanen, M., Rondo,
566 L., Ruuskanen, T., Santos, F. D., Sarnela, N., Schallhart, S., Schnitzhofer, R., Seinfeld, J. H.,
567 Simon, M., Sipila, M., Stozhkov, Y., Stratmann, F., Tome, A., Trostl, J., Tsagkogeorgas, G.,
568 Vaattovaara, P., Viisanen, Y., Virtanen, A., Vrtala, A., Wagner, P. E., Weingartner, E., Wex, H.,
569 Williamson, C., Wimmer, D., Ye, P., Yli-Juuti, T., Carslaw, K. S., Kulmala, M., Curtius, J.,
570 Baltensperger, U., Worsnop, D. R., Vehkamäki, H., and Kirkby, J.: Molecular understanding of
571 sulphuric acid-amine particle nucleation in the atmosphere, *Nature*, 502(7471), 359-363,

572 doi:10.1038/nature12663, 2013.

573 Anttila, T., Kerminen, V. M., Kulmala, M., Laaksonen, A., and O'Dowd, C. D.: Modelling the
574 formation of organic particles in the atmosphere, *Atmos. Chem. Phys.*, 4(4), 1071-1083, doi:
575 10.5194/acp-4-1071-2004, 2004.

576 Asmi, E., Sipilä M., Manninen, H. E., Vanhanen, J., Lehtipalo, K., Gagné S., Neitola, K., Mirme, A.,
577 Mirme, S., Tamm, E., Uin, J., Komsaare, K., Attoui, M., and Kulmala, M.: Results of the first air
578 ion spectrometer calibration and intercomparison workshop, *Atmos. Chem. Phys.*, 9(1), 141-154,
579 doi: 10.5194/acp-9-141-2009, 2009.

580 Brus, D., Neitola, K., Hyvärinen, A.-P., Petäjä T., Vanhanen, J., Sipilä M., Paasonen, P., Kulmala,
581 M., and Lihavainen, H.: Homogenous nucleation of sulfuric acid and water at close to
582 atmospherically relevant conditions, *Atmos. Chem. Phys.*, 11(11), 5277-5287, doi:
583 10.5194/acp-11-5277-2011, 2011.

584 Chan, C. K., and Yao, X.: Air pollution in mega cities in China, *Atmos. Environ.*, 42(1), 1-42,
585 doi: :10.1016/j.atmosenv.2007.09.003.

586 Donahue, N. M., Trump, E. R., Pierce, J. R., and Riipinen, I.: Theoretical constraints on pure
587 vapor-pressure driven condensation of organics to ultrafine particles, *Geophys. Res. Lett.*, 38(16),
588 L16801, doi: 10.1029/2011gl048115, 2011.

589 Donahue, N. M., Kroll, J. H., Pandis, S. N., and Robinson, A. L.: A two-dimensional volatility basis
590 set – Part 2: Diagnostics of organic-aerosol evolution, *Atmos. Chem. Phys.*, 12(2), 615-634, doi:
591 10.5194/acp-12-615-2012, 2012.

592 Ehn, M., Thornton, J. A., Kleist, E., Sipilä, M., Junninen, H., Pullinen, I., Springer, M., Rubach, F.,
593 Tillmann, R., Lee, B., Lopez-Hilfiker, F., Andres, S., Acir, I.-H., Rissanen, M., Jokinen, T.,

594 Schobesberger, S., Kangasluoma, J., Kontkanen, J., Nieminen, T., Kurten, T., Nielsen, L. B.,
595 Jorgensen, S., Kjaergaard, H. G., Canagaratna, M., Maso, M. D., Berndt, T., Petaja, T., Wahner,
596 A., Kerminen, V. M., Kulmala, M., Worsnop, D. R., Wildt, J., and Mentel, T. F.: A large source of
597 low-volatility secondary organic aerosol, *Nature*, 506(7489), 476-479, doi: 10.1038/nature13032,
598 2014.

599 Herrmann, E., Ding, A. J., Kerminen, V.-M., Petäjä T., Yang, X. Q., Sun, J. N., Qi, X. M., Manninen,
600 H., Hakala, J., Nieminen, T., Aalto, P. P., Kulmala, M., and Fu, C. B.: Aerosols and nucleation in
601 eastern China: first insights from the new SORPES-NJU station, *Atmos. Chem. Phys.*, 14,
602 2169-2183, doi: 10.5194/acp-14-2169-2014, 2014.

603 Hirsikko, A., Laakso, L., Horrak, U., Aalto, P. P., Kerminen, V. M., and Kulmala, M.: Annual and
604 size dependent variation of growth rates and ion concentrations in boreal forest, *Boreal Environ.*
605 *Res.*, 10, 357-469, 2005.

606 Jiang, J., Chen, M., Kuang, C., Attoui, M., and McMurry, P. H.: Electrical Mobility Spectrometer
607 Using a Diethylene Glycol Condensation Particle Counter for Measurement of Aerosol Size
608 Distributions Down to 1 nm, *Aerosol Sci. Technol.*, 45(4), 510-521, doi:
609 10.1080/02786826.2010.547538, 2011a.

610 Jiang, J., Zhao, J., Chen, M., Eisele, F. L., Scheckman, J., Williams, B. J., Kuang, C., and McMurry,
611 P. H.: First Measurements of Neutral Atmospheric Cluster and 1-2 nm Particle Number Size
612 Distributions During Nucleation Events, *Aerosol Sci. Technol.*, 45(4), II-V, doi:
613 10.1080/02786826.2010.546817, 2011b.

614 Jokinen, T., Sipilä M., Junninen, H., Ehn, M., Lönn, G., Hakala, J., Petäjä T., Mauldin III, R. L.,
615 Kulmala, M., and Worsnop, D. R.: Atmospheric sulphuric acid and neutral cluster measurements

616 using CI-API-TOF, *Atmos. Chem. Phys.*, 12(9), 4117-4125, doi: 10.5194/acp-12-4117-2012,
617 2012.

618 Junninen, H., Hulkkonen, M., Riipinen, I., Nieminen, T., Hirsikko, A., Suni, T., Boy, M., Lee, S.-H.,
619 Vana, M., Tammet, T., Kerminen, V. M., and Kulmala, M.: Observations on nocturnal growth of
620 atmospheric clusters, *Tellus Ser. B*, 60, 365-371, doi:10.1111/j.1600-0889.2008.00356.x, 2008.

621 Junninen, H., Ehn, M., Petäjä T., Luosujärvi, L., Kotiaho, T., Kostianen, R., Rohner, U., Gonin, M.,
622 Fuhrer, K., Kulmala, M., and Worsnop, D. R.: A high-resolution mass spectrometer to measure
623 atmospheric ion composition, *Atmos. Meas. Tech.*, 3, 1039-1053, doi: 10.5194/amtd-3-599-2010,
624 2010.

625 Kangasluoma, J., Kuang, C., Wimmer, D., Rissanen, M. P., Lehtipalo, K., Ehn, M., Worsnop, D.R.,
626 Wang, J., Kulmala, M. and Petäjä T.: Sub-3 nm particle size and composition dependent response
627 of a nano-CPC battery. *Atmos. Meas. Tech.*, 7, 689-700, doi: 10.5194/amt-7-689-2014, 2014.

628 Kirkby, J., Curtius, J., Almeida, J., Dunne, E., Duplissy, J., Ehrhart, S., Franchin, A., Gagne, S., Ickes,
629 L., Kurten, A., Kupc, A., Metzger, A., Riccobono, F., Rondo, L., Schobesberger, S.,
630 Tsagkogeorgas, G., Wimmer, D., Amorim, A., Bianchi, F., Breitenlechner, M., David, A.,
631 Dommen, J., Downard, A., Ehn, M., Flagan, R. C., Haider, S., Hansel, A., Hauser, D., Jud, W.,
632 Junninen, H., Kreissl, F., Kvashin, A., Laaksonen, A., Lehtipalo, K., Lima, J., Lovejoy, E. R.,
633 Makhmutov, V., Mathot, S., Mikkila, J., Minginette, P., Mogo, S., Nieminen, T., Onnela, A.,
634 Pereira, P., Petaja, T., Schnitzhofer, R., Seinfeld, J. H., Sipila, M., Stozhkov, Y., Stratmann, F.,
635 Tome, A., Vanhanen, J., Viisanen, Y., Vrtala, A., Wagner, P. E., Walther, H., Weingartner, E., Wex,
636 H., Winkler, P. M., Carslaw, K. S., Worsnop, D. R., Baltensperger, U., and Kulmala, M.: Role of
637 sulphuric acid, ammonia and galactic cosmic rays in atmospheric aerosol nucleation, *Nature*,

638 476(7361), 429-433, doi:10.1038/nature10343, 2011.

639 Kuang, C., Chen, M., Zhao, J., Smith, J., McMurry, P. H., and Wang, J.: Size- and time-resolved
640 growth rate measurements of 1 to 5 nm freshly formed atmospheric nuclei, *Atmos. Chem. Phys.*,
641 12(9), 3573-3589, doi: 10.5194/acpd-11-25427-2011, 2012.

642 Kulmala, M., Kerminen, V. M., Anntila, T., Laaksonen, A., and O'Dowd, C. D.: Organic aerosol
643 formation via sulfate cluster activation, *J. Geophys. Res.*, 109, D04205, doi:
644 10.1029/2003JD003961, 2004a.

645 Kulmala, M., Laakso, L., Lehtinen, K. E. J., Riipinen, I., Dal Maso, M., Anttila, T., Kerminen, V.-M.,
646 Hõrrak, U., Vana, M., and Tammet, H.: Initial steps of aerosol growth, *Atmos. Chem. Phys.*, 4(11),
647 2553-2560, doi: 10.5194/acp-4-2553-2004, 2004b.

648 Kulmala, M., Petäjä T., Nieminen, T., Sipilä M., Manninen, H. E., Lehtipalo, K., Dal Maso, M.,
649 Aalto, P. P., Junninen, H., Paasonen, P., Riipinen, I., Lehtinen, K. E. J., Laaksonen, A., and
650 Kerminen, V. M.: Measurement of the nucleation of atmospheric aerosol particles, *Nat. Protocols*,
651 7(9), 1651-1667, doi: 10.1038/nprot.2012.091, 2012.

652 Kulmala, M., Kontkanen, J., Junninen, H., Lehtipalo, K., Manninen, H. E., Nieminen, T., Petäjä T.,
653 Sipilä M., Schobesberger, S., Rantala, P., Franchin, A., Jokinen, T., Järvinen, E., Äijälä M.,
654 Kangasluoma, J., Hakala, J., Aalto, P. P., Paasonen, P., Mikkilä J., Vanhanen, J., Aalto, J., Hakola,
655 H., Makkonen, U., Ruuskanen, T., Mauldin, R. L., Duplissy, J., Vehkamäki, H., Bäck, J.,
656 Kortelainen, A., Riipinen, I., Kurtén, T., Johnston, M. V., Smith, J. N., Ehn, M., Mentel, T. F.,
657 Lehtinen, K. E. J., Laaksonen, A., Kerminen, V. M., and Worsnop, D. R.: Direct Observations of
658 Atmospheric Aerosol Nucleation, *Science*, 339(6122), 943-946, doi: 10.1126/science.1227385,
659 2013.

660 Kulmala, M., Petäjä T., Ehn, M., Thornton, J., Sipilä M., Worsnop, D. R. and Kerminen, V. M.:
661 Chemistry of Atmospheric Nucleation: On the Recent Advances on Precursor Characterization
662 and Atmospheric Cluster Composition in Connection with Atmospheric New Particle Formation,
663 *Annu. Rev. Phys. Chem.*, 65, 21–37, doi: 10.1146/annurev-physchem-040412-110014, 2014.

664 Kürten, A., Jokinen, T., Simon, M., Sipilä M., Sarnela, N., Junninen, H., Adamov, A., Almeida, J.,
665 Amorim, A., Bianchi, F., Breitenlechner, M., Dommen, J., Donahue, N. M., Duplissy, J., Ehrhart,
666 S., Flagan, R. C., Franchin, A., Hakala, J., Hansel, A., Heinritzi, M., Hutterli, M., Kangasluoma,
667 J., Kirkby, J., Laaksonen, A., Lehtipalo, K., Leiminger, M., Makhmutov, V., Mathot, S., Onnela,
668 A., Petäjä T., Praplan, A. P., Riccobono, F., Rissanen, M. P., Rondo, L., Schobesberger, S.,
669 Seinfeld, J. H., Steiner, G., Tomé A., Tröstl, J., Winkler, P. M., Williamson, C., Wimmer, D., Ye,
670 P., Baltensperger, U., Carslaw, K. S., Kulmala, M., Worsnop, D. R., and Curtius, J.: Neutral
671 molecular cluster formation of sulfuric acid–dimethylamine observed in real time under
672 atmospheric conditions, *Proc. Natl. Acad. Sci. U.S.A.*, 111(42), 15019-15024,
673 doi:10.1073/pnas.1404853111, 2014.

674 Lee, S. H., Young, L. H., Benson, D. R., Kulmala, M., Junninen, H., Suni, T., Campos, T., Rogers, D.
675 C., and Jensen, J.: Observations of nighttime new particle formation in the troposphere, *J.*
676 *Geophys. Res.*, 113, D10210, doi: 10.1029/12007JD009351, 2008.

677 Lehtipalo, K., Sipilä M., Riipinen, I., Nieminen, T., and Kulmala, M.: Analysis of atmospheric
678 neutral and charged molecular clusters in boreal forest using pulse-height CPC, *Atmos. Chem.*
679 *Phys.*, 9, 4177–4184, 2009.

680 Lehtipalo, K., Sipilä M., Junninen, H., Ehn, M., Berndt, T., Kajos, M. K., Worsnop, D. R., Petaja, T.,
681 and Kulmala, M.: Nanoparticles in boreal forest and coastal environment: a comparison of

682 observations and implications of the nucleation mechanism, *Atmos. Chem. Phys.*, 10, 7009-7016,
683 2010.

684 Lehtipalo, K., Sipila, M., Junninen, H., Ehn, M., Berndt, T., Kajos, M. K., Worsnop, D. R., Petaja, T.,
685 and Kulmala, M.: Observations of Nano-CN in the Nocturnal Boreal Forest, *Aerosol Sci.*
686 *Technol.*, 45(4), 499-509, doi: 10.1080/02786826.2010.547537, 2011.

687 Lehtipalo., K., Leppä, J., Kontkanen., J., Kangasluoma., J., Franchin., A., Wimmer., D.,
688 Schobesberger., S., Junninen., H., Petäjä, T., Sipilä, M., Mikkilä, J., Vanhanen., J., Worsnop., D.
689 R., and Kulmala, M.: Methods for determining particle size distribution and growth rates between
690 1 and 3 nm using the Particle Size Magnifier, *Boreal Environ. Res.*, 19, 215–236, 2014.

691 Matsui, H., Koike, M., Takegawa, N., Kondo, Y., Takami, A., Takamura, T., Yoon, S., Kim, S. W.,
692 Lim, H. C., and Fast, J. D.: Spatial and temporal variations of new particle formation in East Asia
693 using an NPF-explicit WRF-chem model: North-south contrast in new particle formation
694 frequency, *J. Geophys. Res.*, 118(20), 11,647-611,663, doi:10.1002/jgrd.50821, 2013.

695 McMurry, P. H., Fink, M., Sakuri, H., Stolzenburg, M., Mauldin III, R. L., Smith, J., Eisele, F. L.,
696 Moore, K., Sjostedt, S., Tanner, D., Huey, L. G., Nowak, J. B., Edgerton, E., and Voisin, D.: A
697 criterion for new particle formation in the sulfur-rich Atlanta atmosphere, *J. Geophys. Res.*, 110,
698 D22S02, doi:10.1029/2005JD005901, doi: 10.1029/2005JD005901, 2005.

699 Merikanto, J., Spracklen, D. V., Mann, G. W., Pickering, S. J., and Carslaw, K. S.: Impact of
700 nucleation on global CCN, *Atmos. Chem. Phys.*, doi: 10.5194/acp-9-8601-2009, 9, 8601-8616,
701 2009.

702 Mikkonen, S., Romakkaniemi, S., Smith, J. N., Korhonen, H., Petäjä T., Plass-Duelmer, C., Boy, M.,
703 McMurry, P. H., Lehtinen, K. E. J., Joutsensaari, J., Hamed, A., Mauldin III, R. L., Birmili, W.,

704 Spindler, G., Arnold, F., Kulmala, M., and Laaksonen, A.: A statistical proxy for sulphuric acid
705 concentration, *Atmos. Chem. Phys.*, 11:11319-11334, doi: 10.5194/acpd-11-20141-2011, 2011.

706 Nieminen, T., Lehtinen, K. E. J., and Kulmala, M.: Sub-10 nm particle growth by vapor condensation
707 - effects of vapor molecule size and particle thermal speed, *Atmos. Chem. Phys.*, 10(20),
708 9773-9779, doi: 10.5194/acp-10-9773-2010, 2010.

709 Ortega, I. K., Suni, T., Gronholm, T., Boy, M., Hakola, H., Hellen, H., Valmari, T., Arvela, H.,
710 Vehkamäki, H., and Kulmala, M.: Is eucalyptol the cause of nocturnal events observed in
711 Australia?, *Boreal Environ. Res.*, 14(4), 606-615, 2009.

712 Ortega, I. K., Suni, T., Boy, M., Grönholm, T., Manninen, H. E., Nieminen, T., Ehn, M., Junninen, H.,
713 Hakola, H., Hellén, H., Valmari, T., Arvela, H., Zegelin, S., Hughes, D., Kitchen, M., Cleugh, H.,
714 Worsnop, D. R., Kulmala, M., and Kerminen, V. M.: New insights into nocturnal nucleation,
715 *Atmos. Chem. Phys.*, 12(9), 4297-4312, doi:10.5194/acp-12-4297-2012, 2012.

716 Pierce, J. R., and Adams, P. J.: Uncertainty in global CCN concentrations from uncertain aerosol
717 nucleation and primary emission rates, *Atmos. Chem. Phys.*, 9(4), 1339-1356, doi:
718 10.5194/acp-9-1339-2009, 2009.

719 Riccobono, F., Schobesberger, S., Scott, C. E., Dommen, J., Ortega, I. K., Rondo, L., Almeida, J.,
720 Amorim, A., Bianchi, F., Breitenlechner, M., David, A., Downard, A., Dunne, E. M., Duplissy, J.,
721 Ehrhart, S., Flagan, R. C., Franchin, A., Hansel, A., Junninen, H., Kajos, M., Keskinen, H., Kupc,
722 A., Kürten, A., Kvashin, A. N., Laaksonen, A., Lehtipalo, K., Makhmutov, V., Mathot, S.,
723 Nieminen, T., Onnela, A., Petäjä, T., Praplan, A. P., Santos, F. D., Schallhart, S., Seinfeld, J. H.,
724 Sipilä, M., Spracklen, D. V., Stozhkov, Y., Stratmann, F., Tomé, A., Tsagkogeorgas, G.,
725 Vaattovaara, P., Viisanen, Y., Virtala, A., Wagner, P. E., Weingartner, E., Wex, H., Wimmer, D.,

726 Carslaw, K. S., Curtius, J., Donahue, N. M., Kirkby, J., Kulmala, M., Worsnop, D. R., and
727 Baltensperger, U.: Oxidation Products of Biogenic Emissions Contribute to Nucleation of
728 Atmospheric Particles, *Science*, 344(6185), 717-721, doi:10.1126/science.1243527, 2014.

729 Riipinen, I., Yli-Juuti, T., Pierce, J. R., Petaja, T., Worsnop, D. R., Kulmala, M., and Donahue, N. M.:
730 The contribution of organics to atmospheric nanoparticle growth, *Nature Geosci.*, 5(7), 453-458,
731 doi: 10.1038/NGEO1499, 2012.

732 Russell, L. M., Mensah, A. A., Fischer, E. V., Sive, B. C., Varner, R. K., Keene, W. C., Stutz, J., and
733 Pszenny, A. A. P.: Nanoparticle growth following photochemical α - and β -pinene oxidation at
734 Appledore Island during International Consortium for Research on Transport and
735 Transformation/Chemistry of Halogens at the Isles of Shoals 2004, *J. Geophys. Res.*, 112(D10),
736 D10S21, doi:10.1029/2006jd007736, 2007. Seinfeld, J. H., and Pandis, S. N.: *Atmospheric
737 chemistry and physics: from air pollution to climate change*, 2nd ed., John Wiley and Sons. Inc.,
738 New York, 2006.

739 Schobesberger, S., Junninen, H., Bianchi, F., Lönn, G., Ehn, M., Lehtipalo, K., Dommen, J., Ehrhart,
740 S., Ortega, I. K., Franchin, A., Nieminen, T., Riccobono, F., Hutterli, M., Duplissy, J., Almeida, J.,
741 Amorim, A., Breitenlechner, M., Downard, A. J., Dunne, E. M., Flagan, R. C., Kajos, M.,
742 Keskinen, H., Kirkby, J., Kupc, A., Kürten, A., Kurtén, T., Laaksonen, A., Mathot, S., Onnela, A.,
743 Praplan, A. P., Rondo, L., Santos, F. D., Schallhart, S., Schnitzhofer, R., Sipilä M., Tomé A.,
744 Tsagkogeorgas, G., Vehkamäki, H., Wimmer, D., Baltensperger, U., Carslaw, K. S., Curtius, J.,
745 Hansel, A., Petäjä T., Kulmala, M., Donahue, N. M., and Worsnop, D. R.: Molecular
746 understanding of atmospheric particle formation from sulfuric acid and large oxidized organic
747 molecules, *Proc. Natl. Acad. Sci. U.S.A.*, doi:10.1073/pnas.1306973110, 2013.

748 Sipila, M., Lehtipalo, K., Attoui, M., Neitola, K., Petäjä T., Aalto, P. P., O'Dowd, C. D., and Kulmala,
749 M.: Laboratory Verification of PH-CPC's Ability to Monitor Atmospheric Sub-3 nm Clusters,
750 *Aerosol Sci. Technol.*, 43(2), 126-135, doi: 10.1080/02786820802506227, 2009.

751 Spracklen, D. V., Carslaw, K. S., Kulmala, M., Kerminen, V.-M., Sihto, S.-L., Riipinen, I., Merikanto,
752 J., Mann, G. W., Chipperfield, M. P., Wiedensohler, A., Birmili, W., and Lihavainen, H.:
753 Contribution of particle formation to global cloud condensation nuclei concentrations, *Geophys.*
754 *Res. Lett.*, 35(6), L06808, doi:10.1029/2007GL033038, 2008.

755 Suni, T., Kulmala, M., Hirsikko, A., Bergman, T., Laakso, L., Aalto, P. P., Leuning, R., Cleugh, H.,
756 Zegelin, S., Hughes, D., van Gorsel, E., Kitchen, M., Vana, M., Hörrak, U., Mirme, S., Mirme, A.,
757 Sevanto, S., Twining, J., and Tardos, C.: Formation and characteristics of ions and charged
758 aerosol particles in a native Australian Eucalypt forest, *Atmos. Chem. Phys.*, 8(1), 129-139,
759 doi:10.5194/acp-8-129-2008, 2008.

760 Svenningsson, B., Arneth, A., Hayward, S., Holst, T., Massling, A., Swietlicko, E., Hirsikko, A.,
761 Junninen, H., Riipinen, I., Vana, M., Dal Maso, M., Hussein, T., and Kulmala, M.: Aerosol
762 particle formation events and analysis of high growth rates observed above a subarctic
763 wetland-forest mosaic, *Tellus*, 60(B), 353-365, doi:10.1111/j.1600-0889.2008.00351.x, 2008.

764 Vanhanen, J., Mikkilä, J., Lehtipalo, K., Sipila, M., Manninen, H. E., Siivola, E., Petaja, T., and
765 Kulmala, M.: Particle Size Magnifier for Nano-CN Detection, *Aerosol Sci. Technol.*, 45(4),
766 533-542, doi: 10.1080/02786826.2010.547889, 2011.

767 von der Weiden, S. L., Drewnick, F., and Borrmann, S.: Particle Loss Calculator – a new software
768 tool for the assessment of the performance of aerosol inlet systems, *Atmos. Meas. Tech.*, 2(2),
769 479-494, doi: 10.5194/amt-2-479-2009, 2009.

770 Wiedensohler, A., Cheng, Y. F., Nowak, A., Wehner, B., Achtert, P., Berghof, M., Birmili, W., Wu, Z.
771 J., Hu, M., Zhu, T., Takegawa, N., Kita, K., Kondo, Y., Lou, S. R., Hofzumahaus, A., Holland, F.,
772 Wahner, A., Gunthe, S. S., Rose, D., Su, H., and Pöschl, U.: Rapid aerosol particle growth and
773 increase of cloud condensation nucleus activity by secondary aerosol formation and condensation:
774 A case study for regional air pollution in northeastern China, *J. Geophys. Res.*, 114(D2), D00G08,
775 doi:10.1029/2008jd010884, 2009.

776 Wang, J., and Wexler, A. S.: Adsorption of organic molecules may explain growth of newly
777 nucleated clusters and new particle formation, *Geophys. Res. Lett.*, 11, 2834-2838, doi:
778 10.1002/grl.50455, 2013.

779 Wang, J., McGraw, R. L., and Kuang, C.: Growth of atmospheric nano-particles by heterogeneous
780 nucleation of organic vapor, *Atmos. Chem. Phys.*, 13(13), 6523-6531, doi:
781 10.5194/acp-13-6523-2013, 2013.

782 Xiao, S., Wang, M. Y., Yao, L., Kulmala, M., Zhou, B., Yang, X., Chen, J. M., Wang, D. F., Fu, Q. Y.,
783 Worsnop, D. R., and Wang, L.: Strong atmospheric new particle formation in winter in urban
784 Shanghai, China, *Atmos. Chem. Phys.*, 15(4), 1769-1781, doi: 10.5194/acp-15-1769-2015, 2015.

785 Yu, H., Gannet Hallar, A., You, Y., Sedlacek, A., Springston, S., Kanawade, V. P., Lee, Y. N., Wang,
786 J., Kuang, C., McGraw, R. L., McCubbin, I., Mikkila, J., and Lee, S. H.: Sub-3 nm particles
787 observed at the coastal and continental sites in the United States, *J. Geophys. Res.*, 119(2),
788 2013JD020841, doi: 10.1002/2013jd020841, 2014a.

789 Yu, H., Ortega, J., Smith, J. N., Guenther, A. B., Kanawade, V. P., You, Y., Liu, Y., Hosman, K., Karl,
790 T., Seco, R., Geron, C., Pallardy, S. G., Gu, L., Mikkilä J., and Lee, S. H.: New Particle
791 Formation and Growth in an Isoprene-Dominated Ozark Forest: From Sub-5 nm to CCN-Active

792 Sizes, *Aerosol Sci. Technol.*, 48(12), 1285-1298, doi: 10.1080/02786826.2014.984801, 2014b.

793 Yu, F., and Luo, G.: Simulation of particle size distribution with a global aerosol model: contribution
794 of nucleation to aerosol and CCN number concentrations, *Atmos. Chem. Phys.*, 9(20), 7691-7710,
795 doi:10.5194/acp-9-7691-2009, 2009.

796 Yue, D. L., Hu, M., Zhang, R. Y., Wu, Z. J., Su, H., Wang, Z. B., Peng, J. F., He, L. Y., Huang, X. F.,
797 Gong, Y. G., and Wiedensohler, A.: Potential contribution of new particle formation to cloud
798 condensation nuclei in Beijing, *Atmos. Environ.*, 45(33), 6070-6077,
799 doi:10.1016/j.atmosenv.2011.07.037, 2011.

800 Zhang, K. M., and Wexler, A. S.: A hypothesis for growth of fresh atmospheric nuclei, *J. Geophys.*
801 *Res.*, 107, 4577, doi: 10.1029/2002JD002180, 2002.

802 Zhang, R., Khalizov, A., Wang, L., Hu, M., and Xu, W.: Nucleation and growth of nanoparticles in
803 the atmosphere, *Chem. Rev.*, 112(3), 1957-2011, doi: 10.1021/cr2001756, 2012.

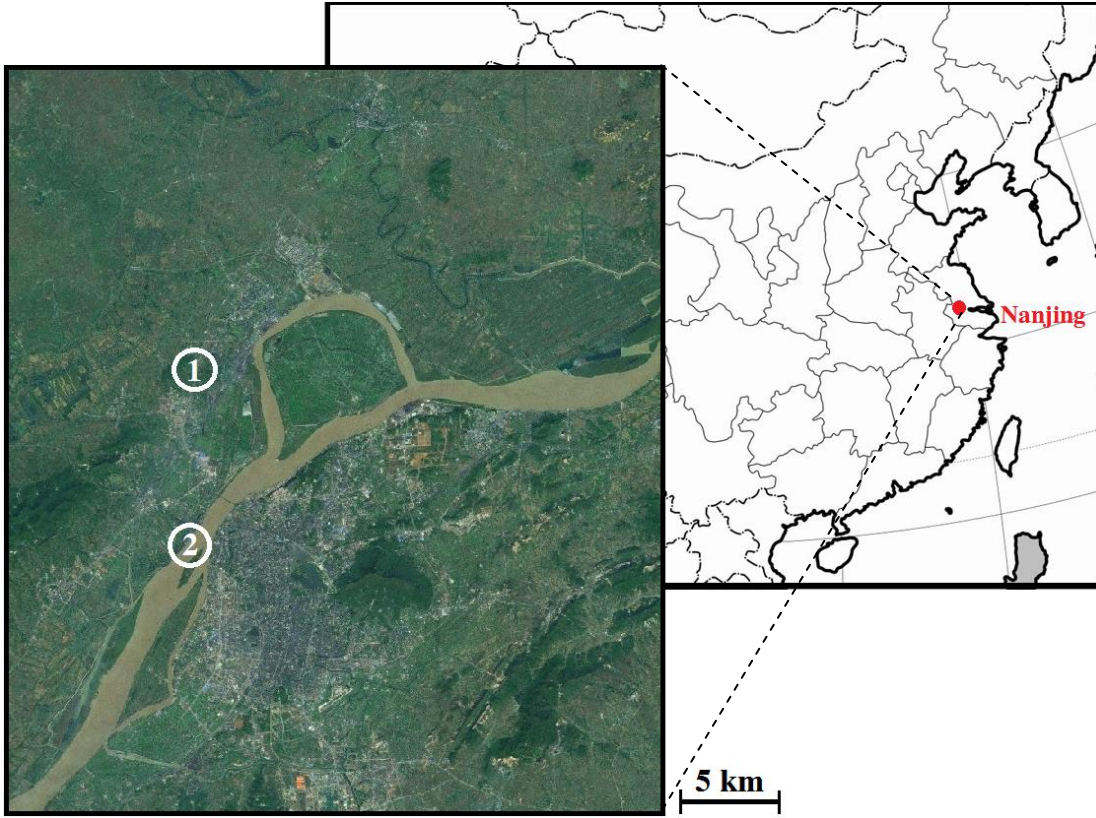
804 Zhao, J., Eisele, F. L., Titcombe, M., Kuang, C., and McMurry, P. H.: Chemical ionization mass
805 spectrometric measurements of atmospheric neutral clusters using the cluster-CIMS, *J. Geophys.*
806 *Res.*, 115, D08205, doi: 10.1029/2009JD012606, 2010.

807

808 Table 1. Activation diameter ($D_{p,act}$), maximum growth rate in 1.4-3 nm ($GR_{max, 1.4-3}$), overall growth rate in 1.4-3 nm ($GR_{1.4-3}$), overall growth
809 rate in 3-20 nm (GR_{3-20}), nucleation rate ($J_{1.4}$), condensation sink (CS), and temperature (T) of selected nucleation events. Estimated gas-phase
810 activating vapor concentrations C_∞ , pure saturation concentration of activating vapor over flat surface C^* , and Mikkonen H_2SO_4 proxy were
811 shown in right 3 columns. All data were for the time periods with maximum nucleation rates.

812

Type	Date	$D_{p,act}$ (nm)	$GR_{max,1.4-3}$ (nm h ⁻¹)	$GR_{1.4-3}$ (nm h ⁻¹)	GR_{3-20} (nm h ⁻¹)	$J_{1.4}$ (cm ⁻³ s ⁻¹)	T (°C)	CS (10 ⁻² s ⁻¹)	Mikkonen H_2SO_4 proxy (cm ⁻³)	C_∞ (cm ⁻³)	C^* (cm ⁻³)
A1	May 15, 2014	2.4	6.4	3.6	7.7	3.0×10 ²	20.8	1.6	8.7×10 ⁷	5.1×10 ⁷	6.3×10 ⁶
A1	Aug 15, 2014	2.4	14.5	7.1	7.7	2.0×10 ²	26.1	1.8	9.3×10 ⁷	1.1×10 ⁸	2.5×10 ⁷
A2	May 16, 2014	2.4	3.8	1.9	0	95	25.3	1.9	1.4×10 ⁸	3.0×10 ⁷	4.0×10 ⁶
A2	May 20, 2014	2.2	2.9	1.6	0	92	24.1	1.9	3.8×10 ⁷	2.3×10 ⁷	2.5×10 ⁶
B1	Feb 18, 2015	1.6	25.9	4.4	6.0	1.1×10 ³	8.2	3.3	3.9×10 ⁷	1.7×10 ⁸	3.5×10 ⁷
B1	Dec 27, 2014	1.6	17.7	4.2	5.5	1.9×10 ²	7.6	2.8	3.5×10 ⁷	1.2×10 ⁸	2.8×10 ⁷
B2	Feb 19, 2015	1.9	25.0	8.9	10.1	8.0×10 ²	7.4	3.2	3.7×10 ⁷	2.0×10 ⁸	5.7×10 ⁷
B2	Mar 4, 2015	1.9	18.0	5.8	8.7	2.5×10 ³	3.9	2.2	4.8×10 ⁷	1.4×10 ⁸	2.0×10 ⁷



813

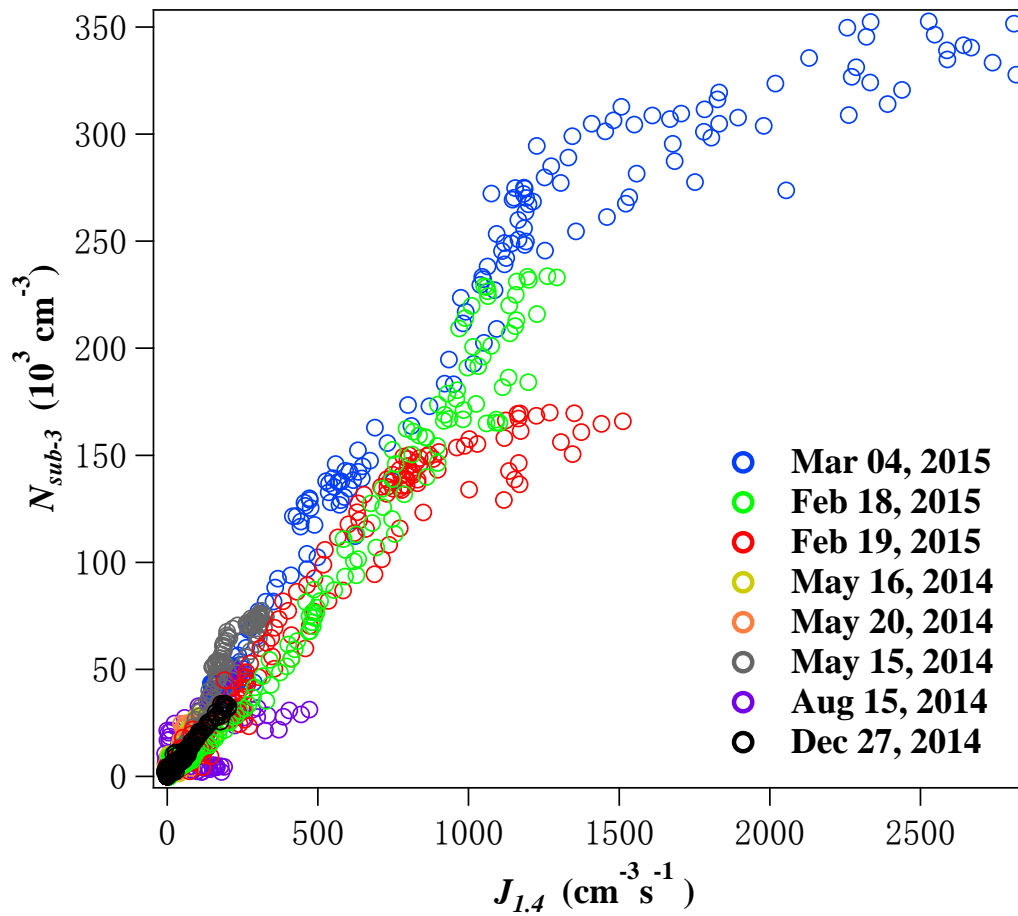
814

815

816

817

Figure 1. Locations of two urban measurement sites in Nanjing, the second largest megacity in the Yangtze River Delta region, China. ① is the NUIST site and ② is the summer measurement site.



819

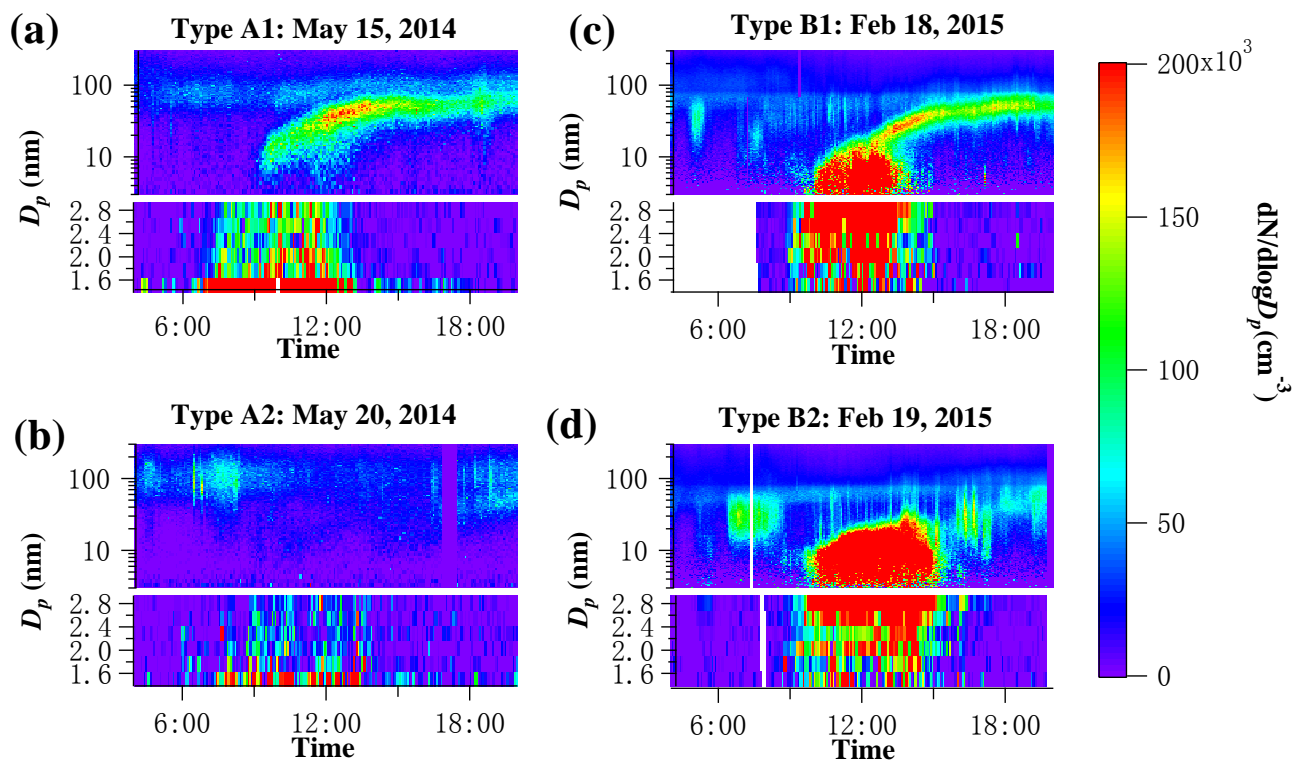
820 Figure 2. N_{sub-3} vs. $J_{1.4}$ in the 8 nucleation events in February, May, December and August during

821 2014-2015. The events were indicated by different colors (blue: March 1, 2015; green: February

822 18, 2015; red: February 19, 2015; purple: August 15, 2014; black: December 27, 2014; grey:

823 May 15, 2014; orange: May 20, 2014; yellow: May 16, 2014)

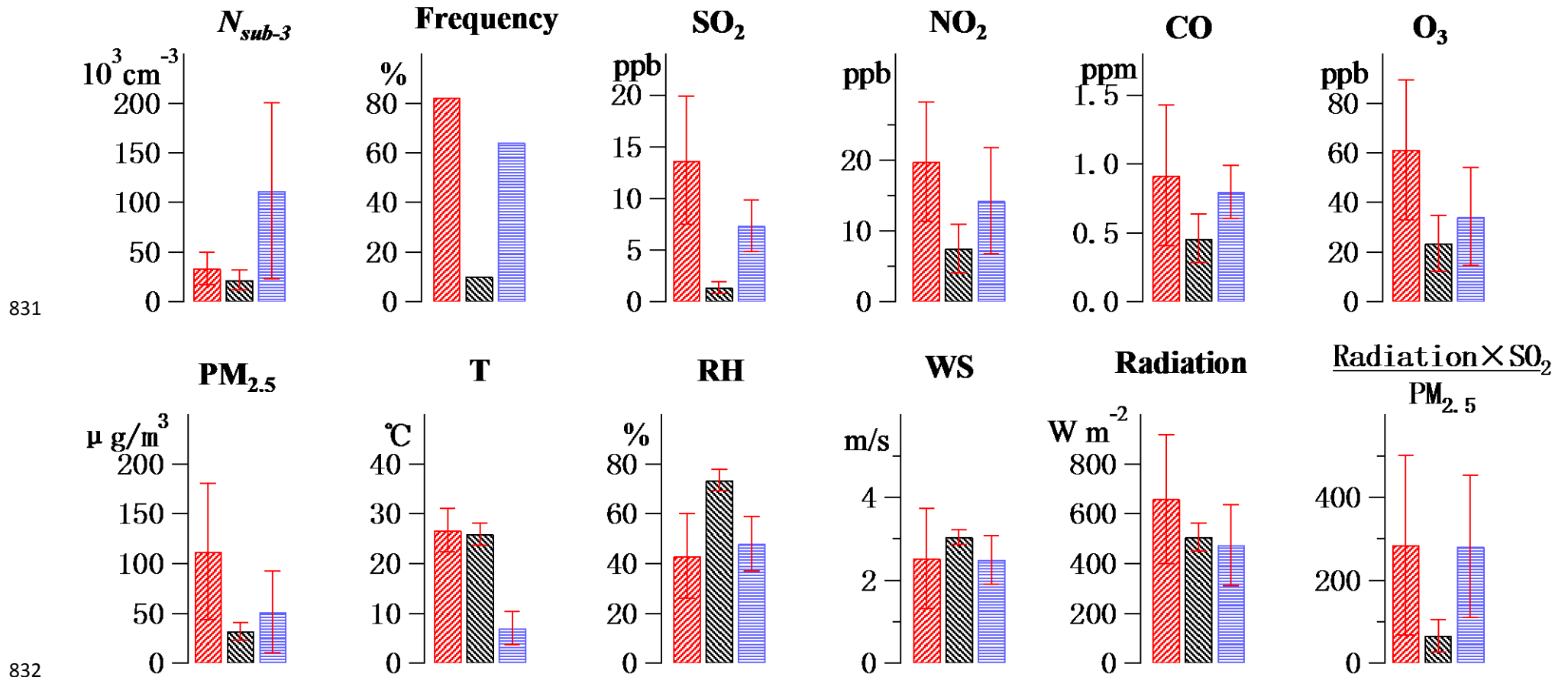
824



826

827 Figure 3. Size spectra of typical (a) Type A1 event on May 15, 2014; (b) Type A2 event on May 20,
 828 2014; (3) Type B1 event on February 18, 2015 and (d) Type B2 event on February 19, 2015 during
 829 our measurement period. Size spectra from 3-300 nm (logarithmic scale) and 1.4-3 nm (linear scale)
 830 were obtained using SMPS and nCNC, respectively.

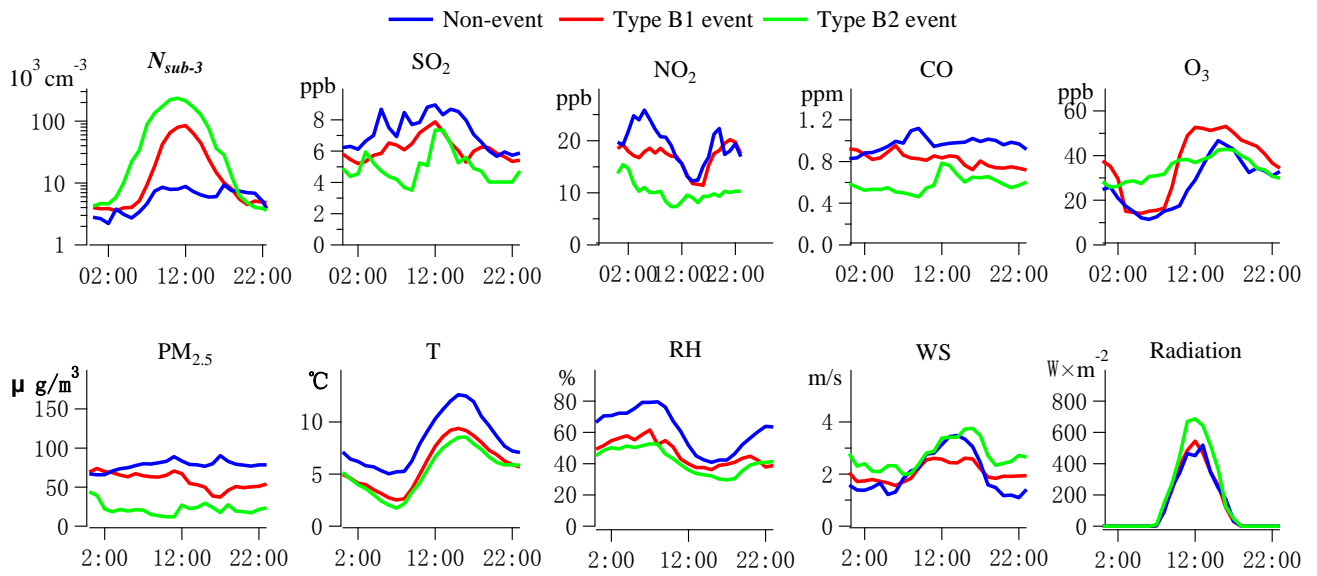
Spring Summer Winter



831

832

833 Figure 4. Mean and standard deviation of event-averaged N_{sub-3} , anthropogenic trace gases (SO_2 , NO_2 , CO and O_3), $\text{PM}_{2.5}$, and meteorological
 834 variables (temperature, RH, wind speed (WS), solar radiation, and radiation $\times \text{SO}_2 / \text{PM}_{2.5}$) for nucleation events in spring (n=17), summer (n=3)
 835 and winter (n=14). Nucleation frequency (the percentage of event days out of total measurement days) was also shown.



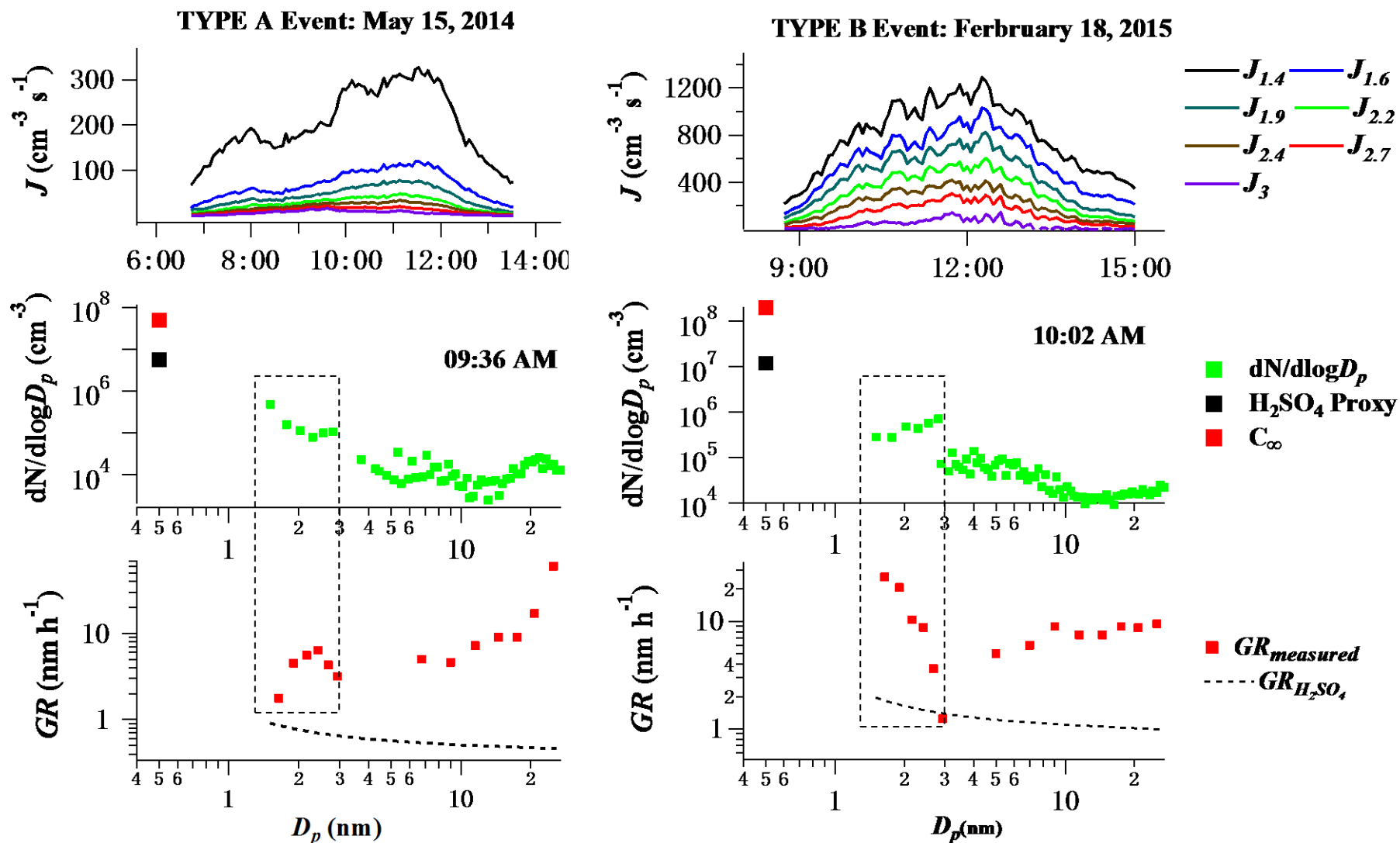
837

838 Figure 5. Diurnal variations of mean N_{sub-3} , anthropogenic trace gases (SO_2 , NO_2 , CO and O_3), $PM_{2.5}$,

839 and meteorological variables (temperature, RH, wind speed, and solar radiation flux) on non-event

840 days (n=8, blue line) and event days (n=3 for Type B1 event, red line and n=6 for Type B2 event,

841 green line) during winter measurement period.



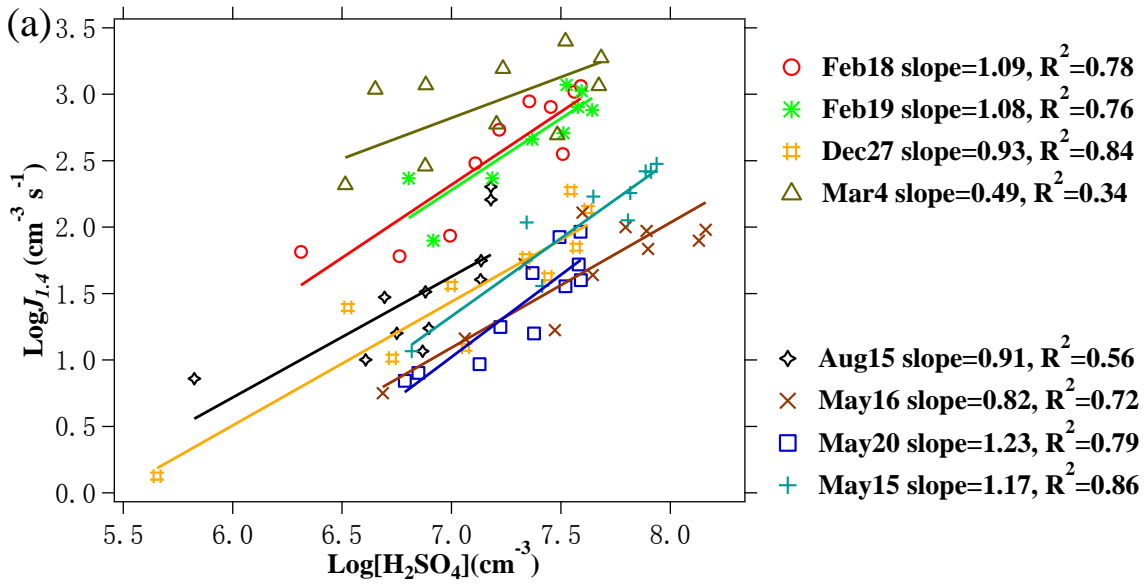
842

843 Figure 6. Upper: formation rates (or equivalently, particle growth fluxes) of 1.4, 1.6, 1.9, 2.2, 2.4, 2.7 and 3.0 nm cluster/particles on May 15

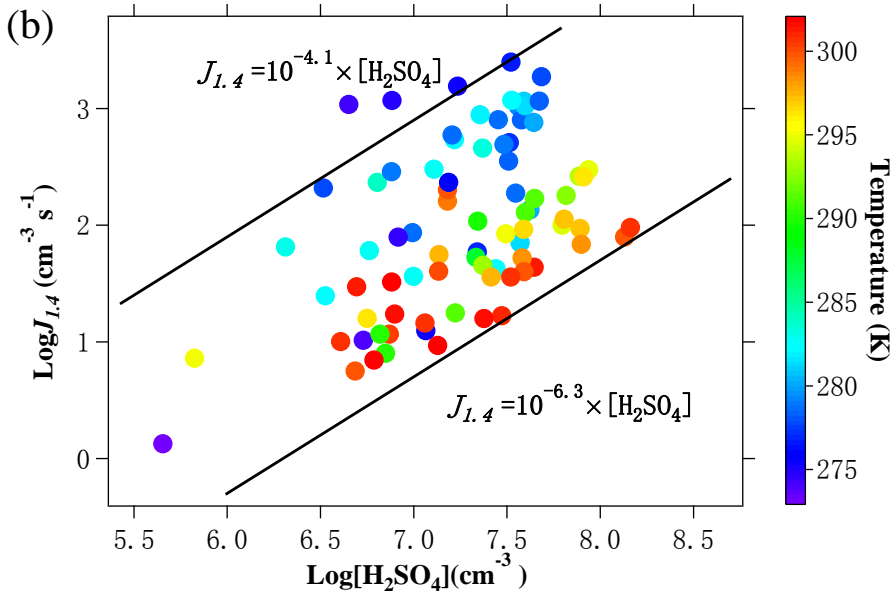
844 2014 (Type A1 event) and Feb 18 2015 (Type B1 event). Middle: particle size distribution ($dN/d\log D_p$, green square) selected during the two

845 events (9:36 AM and 10:02 AM). Lower: particle growth rates measured during the same time periods ($GR_{measured}$, red square). Also shown in the
846 figure were H_2SO_4 proxy (black square) and growth rates calculated from the H_2SO_4 proxy ($GR_{H_2SO_4}$, dashed black line), as well as the
847 calculated ELVOC concentration (C_{∞} , red square) during the same time periods. Dashed boxes in the lower panels highlighted the size
848 distributions and growth rates between 1.4 and 3 nm measured with nCNC.

849

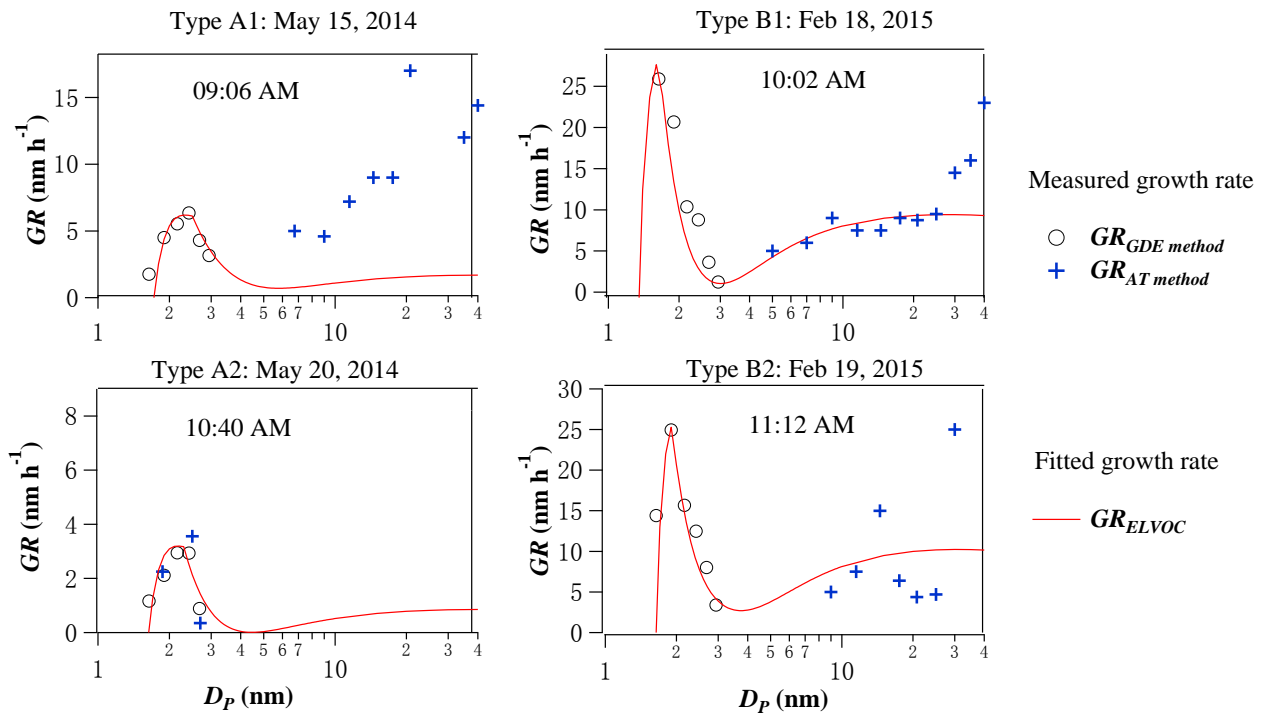


850



851

852 Figure 7. (a) Correlations between $\log J_{1.4}$ and $\log [H_2SO_4]$ for the 8 events. H_2SO_4 proxy was
 853 calculated according to Mikkonen et al. (2011). $J_{1.4}$ and $[H_2SO_4]$ were synchronized to 1 hour that
 854 was the time resolution of solar radiation data. The colored lines showed linear fits to the data of
 855 every single event. (b) The same dataset as (a), but with symbol color to indicate ambient
 856 temperature. Two black lines showed the linear dependences of $J_{1.4}=10^{-4.1} \times [H_2SO_4]$ and $J_{1.4}=10^{-6.3} \times$
 857 $[H_2SO_4]$, between which most of data points located.



859

860

861 Figure 8. Comparisons of measured ($GR_{GDE\ method}$, black circle) and fitted (GR_{ELVOC} , red line) growth
 862 rates from Eq.2 for typical Type A1, A2, B1, and B2 events. Also shown were growth rates
 863 calculated from appearance time method ($GR_{AT\ method}$, blue cross) for sub-3 nm particles when growth
 864 rate was relatively small or for larger particles with large size intervals.

865